Spatial/Temporal Patterns in Weddell Gyre Characteristics and Their Relationship to Global Climate

Douglas G. Martinson[1,2] and Richard A. Iannuzzi[1]

Lamont-Doherty Earth Observatory Palisades, NY, 10964 Department of Earth and Environmental Sciences
Columbia University New York, NY

Abstract. We examine the spatiotemporal variability of the upper ocean-sea ice system of the Atlantic sector of the Southern Ocean subpolar seas (Weddell gyre), and the nature of its covariability with extrapolar climate, identifying teleconnections and their mechanisms. To systematically evaluate the sporadic and sparse distribution of subpolar data we employed an optimal analysis involving Empirical Orthogonal Functions (EOFs). The EOFs reveal that the spatial pattern of coherent spatial covariability of Weddell gyre characteristics is dominated by high interannual variability near the northern (circumpolar) rim of the gyre and lesser variability (10-20% of the variance) in the gyre's central core region. We find considerable, statistically-significant teleconnections between subpolar and extrapolar climate. The dominant link is with ENSO over its broad region of influence, whereby the subpolar upper ocean response is enhanced winter-average cyclonic forcing during tropical warm events (El Niño); the opposite occurs for cold events (La Niña). During El Niño the subpolar gyre contracts so the pycnocline shallows in the gyre center and deepens at the northern rim; sea ice expands northward leading to enhanced surface freshwater in the northern rim. This regional subpolar response is consistent with recent GCM modeling analyses showing that equatorial warm anomalies trigger an increase in the Pacific equator-pole meridional temperature gradient which shifts the subtropical jet equatorward, and farther from the available potential energy of the Antarctic, decreasing the cyclone activity and climatological forcing of the Pacific subpolar gyres. The Pacific equatorial warming also perturbs the Walker cell circulation leading to the opposite response in the Atlantic, resulting in increased cyclonic forcing in the Atlantic's subpolar gyre. We also find that the Weddell gyre interior OAI characteristics covary with sea ice extent in the Atlantic region, and inversely with the sea ice extent in the Amundsen/Bellingshausen regions, reflecting a strong Antarctic Dipole.

1. Introduction

Hypotheses, models and observations suggest that the polar oceans play an important role in global climate through a multitude of polar-unique processes operating over a variety of time scales [e.g., *Walker*, 1923; *Fletcher*, 1969; *Kellogg*, 1975; *Walsh*, 1983; *Chiu*, 1983; *van Loo*n, 1984; *Simmonds and Dix*, 1986; *Mitchell and Hills*, 1986, *James*, 1988; Large *and van Loon*, 1989; *Trenberth et al*., 1990; *Simmonds and Wu*, 1993; *Rind et al*., 1995; *Krishnamurti et al*., 1986; *Imbrie et al*., 1992]. Numerous studies have considered the local/regional interactions between the sea ice and underlying ocean [e.g., *Gordon*, 1981; *Gordon and Huber*, 1984, 1990; *Lemke*, 1987; *Martinson*, 1990], while others have investigated the spatial/temporal distribution of the largest scale teleconnections and mechanisms capable of explaining them at that scale [e.g., *Chiu*, 1983; *van Loo*n, 1984; *Krishnamurti et al*. 1986; *James*, 1988; *Karoly*, 1989; *Meehl*, 1991; *Simmonds and Law*, 1995; *White et al*., 1998; *Peterson and White*, 1998; *Hines and Bromwich*, 1999; *Yuan and Martinson*, 2000a]. Regardless, our documentation and understanding of the detailed nature of the polar-extrapolar teleconnections, and their underlying causal and mechanistic links across the full range of scales (local, regional and global), are still quite rudimentary.

The purpose of this paper is to further document and improve our understanding of the manner by which the polar-extrapolar teleconnections are communicated across the hierarchy of scales involved.

----

[1]Lamont-Doherty Earth Observatory Palisades, NY, 10964

[2]Department of Earth and Environmental Sciences Columbia University New York, NY

2. Approach

Our strategy for documenting and understanding the relationship between variability in the ocean-atmosphere-ice (OAI) system and extrapolar climate, and their linkages across scales, requires the following: (1) quantify the local and regional temporal/spatial variability of climatically-meaningful characteristics of the OAI system (we do so for one of the predominant Antarctic subpolar gyres: the Weddell gyre), (2) correlate the time series of these OAI characteristics to those of extrapolar climate variables and indices, and evaluate the correlation statistics, (3) identify those OAI characteristics that show the most robust links to extrapolar climate and determine the underlying local physical changes responsible for their variability, and (4) evaluate mechanisms consistent with the polar-extrapolar links and observed local OAI changes. This paper develops the methodology and focuses on two primary OAI characteristics, while a companion paper (in preparation) presents the full suite of OAI characteristics and their extrapolar covariability.

2.1 Climate Variables

2.1.1 OAI System Parameters.

We adopt the climatically-meaningful OAI characteristics as quantified through the bulk property parameters of *Martinson and Iannuzzi* [1998; hereafter *MI98*]. *MI98* focus on robust and relatively long-lived information contained within the upper ocean structure. Specifically, vertical integration of temperature (T) and salinity (S) profiles provide bulk property distributions which are used directly, or in combinations, to provide fundamental OAI information on ocean ventilation, water column stability and sea ice growth constraints.

The OAI parameters are dominated by two bulk properties: (1) a "thermal barrier" (TB_w), which is the enthalpy relative to the freezing point available within the permanent thermocline; and (2) a "salt deficit" (SD_w), which is the freshwater surplus in the winter surface layer relative to the deep water (in terms of buoyancy, allowing for the nonlinear equation of state, vertical salt flux, etc.; see *MI98* for details). SD_w must be eliminated by salt input in order to destabilize the surface layer and drive catastrophic overturn. TB_w is the sensible heat that must be vented during erosion of the pycnocline, accompanying elimination of SD_w. As it is vented, this heat stabilizes the water column by melting ice or, equivalently, by preventing ice growth which would otherwise destabilize through salt rejection. Over seasonal time scales, SD_w is reduced by salinization during ice growth, initiating static instability that drives an entrainment heat flux venting TB_w, and freshening and restabilizing (to some degree) the surface layer through ice melt. TB_w thus provides a negative feedback to the ice growth-driven destabilization process.

For practical purposes SD_w and TB_w are normalized into equivalent units of effective ice thickness per unit area. As such, SD_w reveals the thickness of *in situ* ice growth required to reject enough salt to destabilize the surface layer; TB_w reveals the thickness of ice that could be melted by completely venting the thermocline, and it indicates the potential to resist overturn due to the heat storage in the thermocline (i.e., delivered by circumpolar deepwater, CDW).

In various combinations TB_w and SD_w provide the basis for additional parameters of interest. Here we focus on two climatically-relevant parameters: (1) bulk stability, $\Sigma = TB_w + SD_w$, and (2) total ocean heat flux, F_T. Bulk stability is the maximum amount of *in situ* ice growth, or latent heat loss, that the upper ocean can support before destabilizing the water column, flipping the system to its unstable (thermal) mode of *Gordon*, 1991, and generating open ocean deep water formation and preventing winter ice growth, *Martinson* [1990]. Essentially, Σ provides an indication of the total amount of surface buoyancy stabilizing the surface water column and allowing sea ice to form at all. It places an upper limit on *in situ* ice growth.

Total ocean heat flux, F_T, is the sum of turbulent diffusive (F_D) and entrainment (F_E) heat fluxes entering the surface ocean mixed layer across its base. These heat flux components are determined as follows. The external forcing for winter ice growth, F_L, is the upward flux of heat at the bottom of the atmosphere, F_a, less the upward flux of oceanic sensible heat into the mixed layer created by turbulent diffusion; so $F_L = F_a - F_D$. Seasonally-averaged values (indicated by $<>$) of these fluxes dictate the entrainment heat flux $<F_E>$ occurring when surface convection, driven by F_L induced ice growth salinization forces entrainment into the mixed layer of warm underlying pycnocline waters. Specifically, $<F_E> = <F_L>TB_w/\Sigma$. TB_w/Σ indicates what fraction of the initial latent heat of fusion is converted, by the negative feedback, into sensible heat.

The diffusive heat flux $<F_D>$ is parameterized as proportional to the thermal gradient (∇T) through the thermocline, so $<F_D> = <k_T>\rho c_p\overline{\nabla T}$, where $\overline{\nabla T}$ is the depth-averaged ∇T through the thermocline, ρ is the density of seawater (1027.5 kg/m^3), and c_p its heat capacity (4.18×10^3 J/°Ckg). The seasonally-averaged winter turbulent diffusivity coefficient, $<k_T>$, across the pycnocline is rather large in the Antarctic (see *MI98*), 0.66×10^{-4} m^2/s, reflecting small values during quiescent periods averaged with substantially increased values during frequent intense polar lows [*Stanton*, personal communication]. The total ocean sensible heat flux is $<F_T> = <F_E> + <F_D>$. $<F_T>$ estimated in this manner shows excellent agreement to the seasonally measured value of *McPhee et al.*, [1999].

Additional insights regarding the nature of the ocean-ice interaction are provided by other combinations of SD_w and TB_w. These are described and their variability evaluated in the companion paper.

For geometrically ideal T and S profiles, TB_w and SD_w are computed from simple algebraic relationships. These show that the parameters are functions of the following physical characteristics (external system parameters) of the upper water column: S_{ml}, z_{ml}, T_{pp}, S_{pp}, z_{pp} (heat fluxes also depend on k_T, F_L); z indicates a depth, and subscripts indicate the quantity's value within the mixed layer (ml) or at the base of the permanent pycnocline (pp). These algebraic expressions allow us to quantify the degree to which individual external parameters are controlling variability observed in the climatically-meaningful bulk parameters. This defines their sensitivity and allows us to relate local water column changes to regional or global scale forcings (helping identify and/or constrain plausible mechanistic links).

MI98 provide 25-year climatologies for each of the bulk property parameters within the Weddell gyre region (polar gyre from the Antarctic Peninsula to approximately 20° E, spanning the Weddell-Enderby Basin). They are based on historical CTD data from 28 cruises, involving 1423 hydrographic stations (of 1710) that survived considerable quality control and error analysis. The spatial variability in the climatologies have a spatial signal to noise ratio (S/N) of 20 db. Here we determine the variability (detrended yearly anomalies) about these climatological means, as a function of year and location within the gyre, focusing on Σ and $<F_T>$. These anomalies provide the means for comparing the temporal and spatial variability of the OIA interactions in the interior of the polar gyres to that of extrapolar climate variables and indices.

2.2 Extrapolar Climate.

Extrapolar climate variability is measured through a wide variety of existing variables and indices. *Yuan and Martinson* [2000a; hereafter *YM00*] examined the relationship between 20-year records of detrended anomalies in the Antarctic monthly sea ice edge position (SIE^*) and: (1) detrended surface air temperature (SAT^*) at 5°x5° intervals throughout the globe based on National Center for Environmental Forecast (NCEP) and National Center for Atmospheric Research (NCAR) reanalysis surface air temperature at the 1000 Mb pressure level [*Kalnay et al.*, 1996]), (2) SIE^* in 12° contiguous longitude bands (representing the lateral SIE^* decorrelation length) around Antarctica, and (3) large-scale climate indices such as NINO3 (an ENSO-related index based on eastern equatorial Pacific sea surface temperature, SST, averaged in 5° N to 5° S and 150°W to 90°W and robust index for ENSO variability; *Cane et al.*, 1986), the Pacific-North America teleconnection index (PNA), North Atlantic Oscillation index (NAO), and Southern Oscillation Index (SOI), as well as several other indices. *YM00* found considerable, statistically-significant global, circumpolar and index correlations — almost twice as many strong global correlations (teleconnections) as would be expected by correlating noise time series with similar spectral coloring and quasi-periodic components as displayed in the actual SIE^* records.

YM00 performed extensive statistical analysis of the correlations between SIE^* and extrapolar climate, assessing the robustness and likelihood of the links between extrapolar climate and variability in the circumpolar belt around Antarctica. Hoping to draw on that statistical foundation, we use the same climate variables and indices in this study, as well as SIE^*. The latter allows us to determine the extent to which the OAI interactions within the interior of the polar gyre are related to that of the circumpolar margins, as indicated by the ice extent anomalies around the gyre rim.

3. Methods

Several studies [e.g., *van Loon and Shea*, 1985; *Carleton*, 1988; *Gloersen*, 1995; *Ledley and Huang*, 1997; *YM00*; *Simmonds and Jacka*, 1995; *Stammerjohn and Smith*, 1997] have demonstrated a relationship between the subpolar seas and ENSO; perhaps not surprising given the global spatial influence of ENSO [e.g., *Ropelewski and Halpert*, 1987]. Thus, to test the feasibility of our approach, we begin by examining the relationship between ENSO and bulk stability (Σ) and ocean heat flux ($<F_T>$) as computed near the center of the Weddell gyre where the observations are most dense. As seen in Figure 1, Σ and $<F_T>$, averaged annually within a spatial domain encompassing Maud Rise, from 59° - 63° S and 20°W - 8°E. For years in which data exist, the OIA parameters appear to be well correlated with ENSO (r = 0.95 and -0.80 for Σ and $<F_T>$, respectively; significant at the 99.98% and 95% confidence levels (see Appendix for discussion of bootstrap method used to determine significance). The correlations are highly significant, even despite the relatively few data points and sparse, irregular distribution. Note that despite the apparently large scatter of $<F_T>$ in Figure 1 relative to that of Σ, $<F_T>$ has a

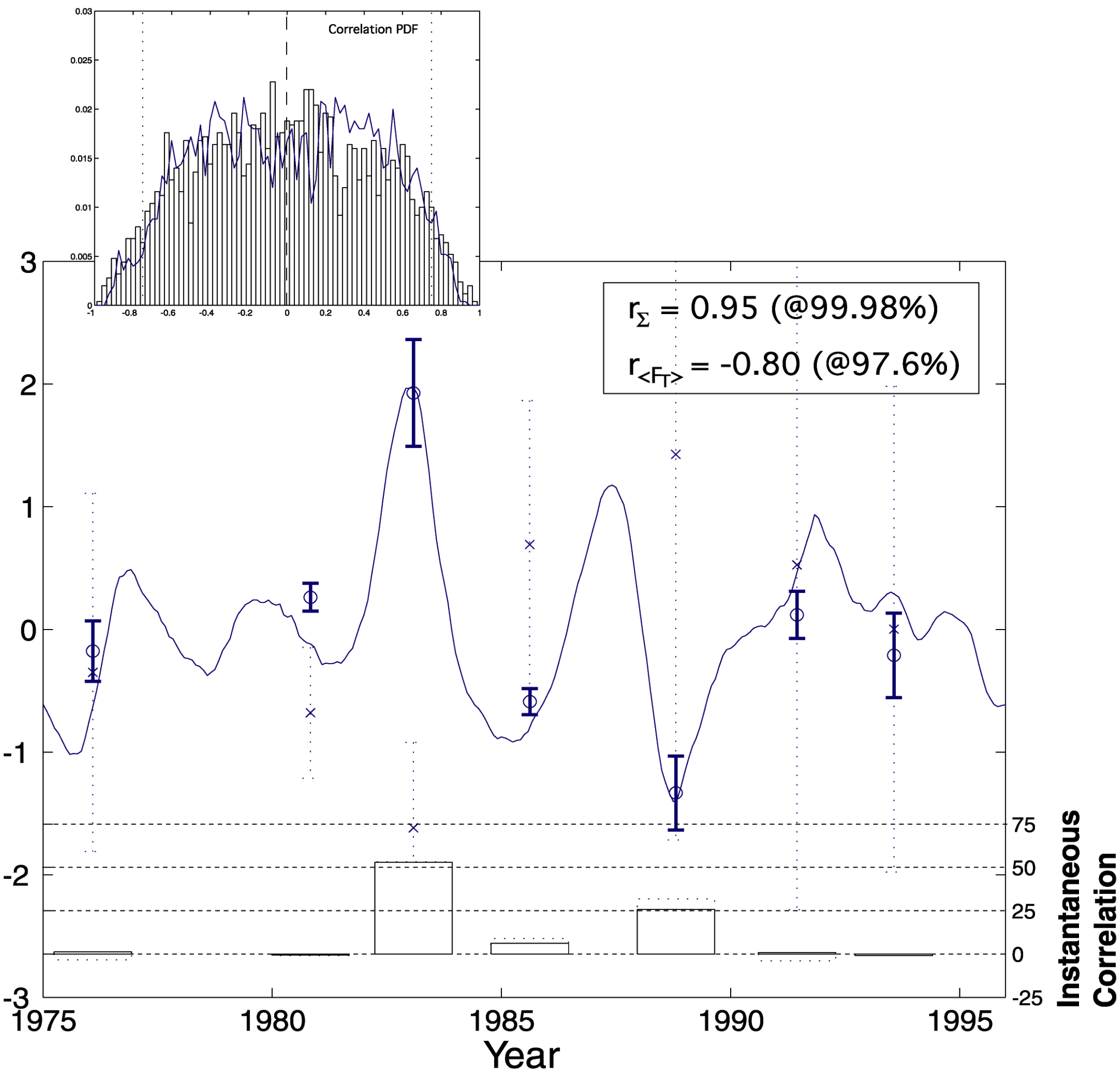

Figure 1. Solid line is NINO3 index of ENSO phenomenon; circles are bulk stability (Σ) from central Weddell gyre region (yearly averages from within 20° W - 8° E and 59° - 63° S spatial domain); crosses are total winter average ocean heat flux ($<F_T>$) from the same region as Σ. Ordinate for all three time series is given on left of figure in z-scores (standard deviations from mean values). Error bars on Σ and $<F_T>$ points reflect scatter within spatial domain. r_Σ gives the degree of linear correlation between NINO3 and Σ and $r_{<F_T>}$ between NINO3 and $<F_T>$. Confidence level of correlations (presented following @ symbol) are determined from bootstrap PDF (inset). Instantaneous correlations (r'; see Appendix for details) given as function of abscissa by boxes at lower portion of figure show percent contribution of each pair of points to overall correlation (solid r' for bulk stability; dashed r' for $<F_T>$).

coefficient of variation (ratio of standard deviation to mean), of 0.36, so the scatter in $<F_T>$ is still reasonably small relative to the domain's mean $<F_T>$ value.

The instantaneous correlation (r'; see Appendix for description), shown in the lower portion of the plot in Figure 1, reveals that the strong correlations are dominated by the fact that the OAI parameters covary most strongly during the extreme ENSO events of 1984 and 1989 — the close correspondence during these years overwhelmingly accounts for the high degree of correlation. Unfortunately, we do not have long enough records to determine if this indicates that the correlation (assuming it to be causal) reflects a mechanism that is only operative when extreme events occur, or whether the mechanism is operative all the time, but dominated by the large variance events as dictated by the construction of a correlation coefficient. Results of Figure 1 suggest that El Niño years are accompanied by anomalously strong bulk stability and low ocean heat flux, and vice versa in La Niña years. This negative covariation works to offset their local OAI impact (see Section 5 for more discussion).

The covarying relationships found here are tantalizing enough to warrant more rigorous investigation. Unfortunately, elsewhere in the Weddell gyre the data are too sparse and sporadic, with low S/N, to extend this analysis. Furthermore, the short length of the time series make their actual and long-term physical significance questionable (though their true statistical significance for their length is well determined by the bootstrap method employed above).

In order to facilitate further analyses and enhance S/N, we interpolate the data of the Weddell gyre region onto a grid that allows direct application of standard analysis tools, including characterization of the spatial/temporal patterns through EOF analysis. Since interpolation may introduce methodological errors into our findings we further investigate results arising from the gridded (interpolated) data by repeating the relevant analysis using the uninterpolated data, and examining (to the extent possible) the degree to which the primary correlations and patterns are preserved. In this manner we eliminate correlation attributed to the interpolation process itself, but still gain the benefits of working with evenly sampled series.

3.1 Optimal Analysis

We use the reduced space optimal analysis (OA) scheme of *Kaplan et al.* [1998; hereafter, *KKCB98*] to produce a smoothly interpolated data set that best preserves the coherent spatial/temporal structure already inherent in the data. The OA method involves the following steps (see *KKCB98* for complete details): (1) define a grid consistent with the gyre dynamics and data distribution; (2) estimate average bulk property values in each grid cell for each year; (3) estimate the sample covariance matrix ($\hat{C}$; hereafter referred to as the covariance matrix, ignoring the "sample" qualifier) for the series in the grid (i.e., quantify how the data covary in space and time across the sampled domain); (4) compute the empirical orthogonal function (EOF) structure from the covariance matrix, representing a physically-consistent basis for the observations, where the lower order EOFs represent spatially-coherent structures whose shapes are preserved through time; (5) reduce the space (increasing S/N) by throwing away those EOFs that represent uncorrelated noise, spatially-localized signal or describe little total variance; (6) combine the surviving (dominant) EOFs to provide a smooth, reduced-space interpolant for the data across the grid in space and time; and (7) interpolate the data using an objective function that optimizes the fit of the preserved EOFs to the data for each year, while preserving a low-order time-varying component described by an autoregressive (AR) order one process (a Markov process). The objective function of the last step assures that the interpolation not only provides the best optimal fit of the EOFs in space at any one time, but that it also avoids any abrupt (presumably unnatural) temporal shifts in the EOF amplitude from one year to the next. Once the data have been interpolated, so as to provide a densely-populated data matrix (except for years in which data does not exist anywhere across the grid: 1979, 1980, 1982, 1987, 1988, 1991 in our 25 year period), the covariance of this matrix is decomposed to provide the full modal structure of EOFs with their time-varying amplitudes indicated by their principal components, PCs. Years for which no data exist are further interpolated by fitting the PCs using both linear and cubic spline interpolants (we evaluate the sensitivity of all correlation results according to which interpolant, linear or spline, is used to fill gaps in the PCs — results suggest negligible sensitivity to this).

The optimal analysis provides an ideal internally-consistent means of utilizing sparse historical data, but it is sensitive to a number of factors. One factor is the uncertainty in the original data. This uncertainty reflects a combination of the scatter in individual estimates of the bulk parameters lying within any one grid cell for a given year, as well as the individual precision in each estimate reflecting the uncertainties propagated through analysis of an individual profile (both uncertainties are accounted for in the averaging process). This uncertainty is quantitatively tracked through the OA process, as it defines an error matrix. More subtle is the sensitivity to the actual grid chosen, as well as to the construction and normalization of the dispersion matrix used to determine the EOF basis for the interpolant. For example, use of a correlation matrix instead of covariance matrix emphasizes covarying structure independent of absolute amplitudes; important if we expect that some region of the gyre may naturally display larger amplitude variability than other regions. In addition, the manner in which the statistical moments are estimated for the covariance matrix elements (e.g., normalizing to a full domain mean, versus grid-specific means) influence the resulting EOFs and the interpolation. Sensitivity to these constructs are investigated.

3.1.1 Gridded Data.

The grid structure for the Weddell gyre spatial domain must be consistent with the gyre dynamics and the general spatial structure of the upper ocean property distributions. This assures that averaging quantities within individual grid cells makes physical sense. In order to develop the grid we examined individual cruise tracks, as well as the climatologies of *MI98* in an effort to locate fronts, abrupt property transitions and regions of maximum lateral property gradients; where properties varied more smoothly, we determined spatial decorrelation lengths. The former reveal natural grid cell boundaries and, in their absence, the latter constrains grid cell size. The latter also helps define length scales required to avoid EOF aliasing [*North et al.*, 1982]. This analysis suggests a physically-optimal configuration as shown in Figure 2. Unfortunately, the physically-optimal grid includes cells for which insufficient data exist to provide robust estimates of the parameters and a stable covariance matrix. To alleviate the problem we combined grid cells until we achieved a grid distribution (Figure 2, combined cells are revealed by common cell number) that consists of 16 spatial grid cells which preserves, to the extent possible, the natural property boundaries of the optimal grid and is compatible with the data density. The latter is satisfied by obtaining a stable covariance matrix as defined by the fraction of negative eigenvalues in the EOF decomposition (negative values reveal a violation of the positive semi-definite criterion and reveals an internally-inconsistent estimate of the covariance matrix).

We compute the various OAI parameters and local physical characteristics using 1423 CTD upper ocean profiles (see Figure 2 for station locations, independent of time), existing from 1972 to the present. Outliers in individual parameter estimates are identified as lying three or more standard deviations from that year's mean value in any particular grid cell; they are eliminated prior to averaging and constitute ~5% of the total data. We then average all remaining values that lie within a grid cell existing for each year. This provides us with "super-data": averaged values for different grid cells and different years. The super-data for each parameter occupy a sparse data matrix, $\mathbf{T}^{o}$; only those cells for years in which data exist within the cell are occupied. The error, as a standard deviation of each super-datum value, is determined during the averaging process; cells 1 and 2 in the grid are poorly sampled.

3.1.2. Covariance Matrix and EOF Decomposition.

Given the reference grid, covariance matrices, $\hat{\mathbf{C}}$, were estimated for each super-data matrix, $\mathbf{T}^{o}$ (one matrix for each parameter evaluated) Covariances involve standardization to local temporal means and standard deviations of the quantity within each particular grid cell. They are estimated by computing biased (because of the limited data) covariance between time series from all pairs of grid cells, involving mutually occupied years only. As suggested by *KKCB98*, application of a spatial filter to the data, or comparably, to the covariance matrix directly (to bypass problems associated with data gaps present in the original data) stabilizes $\hat{\mathbf{C}}$ when constructed in data-poor regions, as is the case here. However, we find this filtering to artificially alter the nature of the covariance too much. It also adds considerable sensitivity to the PCs, though the EOF spatial structures are little influenced. As the analysis is critically dependent upon the PCs we do not perform any filtering of the covariance matrix in our analysis.

Once the covariance matrix is estimated, its

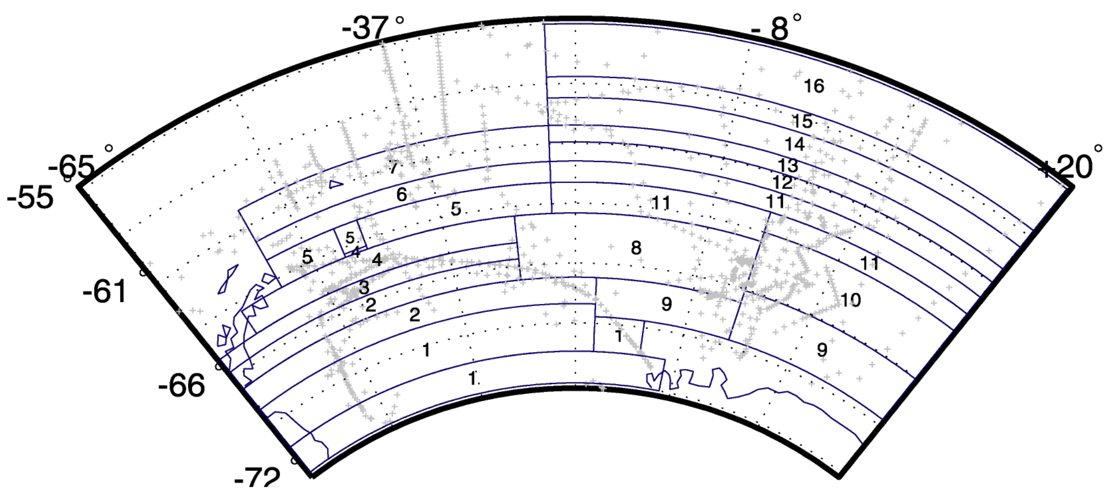

Figure 2. Grid scheme for the optimal analysis of the historical data of the Weddell gyre spatial domain. Individual grid cells reflect ideal physically-consistent grid. Cells sharing same grid-cell number have been merged into singe cells to produce the most stable physically-consistent grid (used for the primary analysis in the paper). Station data used in analysis are indicated by light dots.

eigenvector structure is computed to obtain the EOFs. We examine scree plots to determine the EOF noise floor and preserve, for the interpolant, all EOFs lying above the noise floor, typically the 3 leading EOFs. In most cases, the first 1-3 EOFs describe the vast majority of the total variance (recognizing the caution of *North et al.*, 1982, these leading EOFs do not contain or split pseudo-degenerate multiplet sets). Once the EOFs are determined, we can use those that are preserved as a reduced-space interpolant basis, apply the objective function to interpolate the super-data, producing a smoothed, gridded data matrix, $\hat{\mathbf{T}}$. From the covariance matrix of $\hat{\mathbf{T}}$ we compute the full set of EOFs and their PCs. As expected, the lowest order EOFs are nearly identical to those originally used in the interpolation, but now, with the full matrix we can recover their temporally-varying expansion coefficients in the PCs and the complete internally-consistent modal structure for the observations.

3.2 Uncertainties

3.2.1 Super-Data Uncertainties.

We estimate uncertainties in the bulk parameters used in the super-data as described fully in *MI98*. These provide an estimate of how noise in the individual realizations of T and S profiles manifests itself as uncertainties in the specific bulk parameter values.

3.2.2 Interpolation Error.

Several errors are investigated regarding the interpolation. The most fundamental error is the synthesis error, or interpolation precision, σ_s, reflecting the smooth fit of the reduced-space interpolant. It is given as: $\sigma_s = \mathrm{Var}[\hat{\mathbf{T}}-\mathbf{T}^o]^{1/2}$ (where $\mathrm{Var}[\mathbf{X}] = \mathrm{E}[(\mathbf{X}-\mathrm{E}[\mathbf{X}])(\mathbf{X}-\mathrm{E}[\mathbf{X}])^T]$) for the mutually populated cells only — in other words, how well does the interpolant fit the super-data in each grid cell (illustrated by vertical discrepancies between the circles and bold crosses in Figure 3), averaged over the different years. More important is the interpolation accuracy, σ_a; that is, with what fidelity does the interpolant fill gaps. We estimate interpolation accuracy (*KKCB98*'s truncation error) by eliminating a single super-datum point, and repeating the interpolation process (illustrated by vertical discrepancies between the bold crosses and x's in Figure 3). From this, we evaluate $\varepsilon_{a,i} = (\hat{\mathbf{T}}-\mathbf{T}^o)_{n,m}$ where n, m indicate the error evaluated at the eliminated super-datum element only. We repeat this process, each time eliminating a different datum after replacing the previously eliminated datum (the data are not dense enough to afford the luxury of withholding a significant portion of the data from the original interpolation). After this has been done for each super-datum point, the full suite of ε_a values are evaluated for the average rms accuracy error between the interpolated value at the missing datum and the true (eliminated) values as $\sigma_a = \mathrm{Var}[\varepsilon]^{1/2}$.

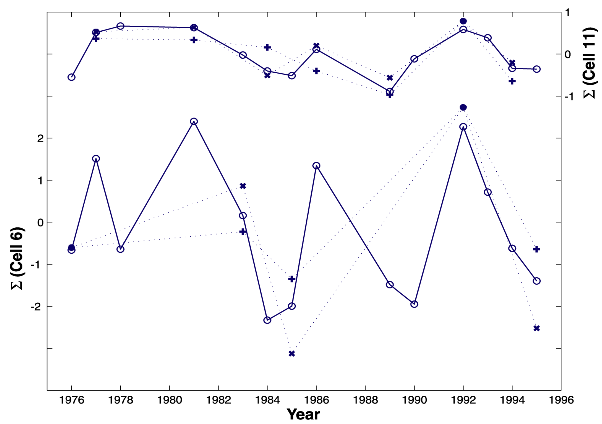

Figure 3. Standardized Σ time series for grid cells 6 (lower curve) and 11 (upper curve); see Figure 2 for cell locations. Bold crosses show original averaged values in cell (super-data values); circles connected by dashed lines show reduced space interpolation involving 3 leading EOFs (not exact fit to super-data because of space reduction); bold x's indicate interpolated values when the super-datum at that time was eliminated from the data base prior to the OA interpolation, thus it gives an indication of how well interpolant can fill temporal gaps in data base.

Treating bulk stability as representative, we find that $\sigma_s = 0.68$, while $\sigma_a = 1.32$. This suggests that the accuracy is just better than twice the precision — in other words, the interpolated values in regions missing data are, on average, likely to lie within two standard deviations of the scatter (precision) of the data throughout the domain. As might be expected, the accuracy error shows spatial variability, reflecting the fact that gaps are filled better in regions that show strong covariability to neighboring cells across the domain, or in regions of denser surrounding data. Figure 3 gives results from two grid cells: one (cell 11) is densely sampled, the other (cell 6) is sparsely sampled.

Uncertainties associated with the sensitivity of the method to the nature of the covariance matrix, grid definition and normalization constants are assessed via sensitivity experiments. Specifically, we repeated the analysis using different grid schemes (including: zonal, meridional, and higher density), and different normalization schemes (including: a full-domain spatial mean, correlation versus covariance). Results of these different experiments suggest to us that the results presented in the next section are fairly robust with respect to the interpolant. More importantly, the changes obtained in EOF patterns did not alter the relative spatial distribution of variability across the domain. However, we estimate a more significant sensitivity in the PCs. Fortunately, the implications of this last number are largely circumvented since we use the PC correlations with extrapolar climate variables/indices to guide further investigation with the non-interpolated data (super-data), as mentioned previously. Most importantly, as an exploratory device, the sensitivities in the results did not suggest any alternate investigations with the non-interpolated data, other than those suggested in the primary analysis.

Finally, the nature of the EOF basis depends on the quality of the covariance matrix we estimate for the data across the grid. Ideally, $\hat{\mathbf{C}}$ is estimated directly from the quadratic operation on the grid's fully-populated data matrix, $\mathbf{T}^o$. Instead, our data are insufficient for this so we must estimate $\hat{\mathbf{C}}$ directly. This allows admittance of inconsistent structure (violation of the positive semi-definiteness). Therefore, the presence of negative eigenvalues reveals inconsistencies in our estimates of how different series across the grid covary. We determine where such inconsistency arises, thus identifying which grid cells are yielding the poorest estimates of covariance, and reducing the overall quality of our EOF decomposition and external correlations. We do this by repeatedly subjecting individual values within a correlation matrix to random perturbations and assessing their probabilistic influence on the degree of negativity in the eigenvalues. We work with a correlation matrix in this case to constrain the magnitude of the random perturbations, but given the relatively small spatial domain, the EOF structure is little altered from that obtained from the covariance matrix. From this we identify those cells with the biggest impact, and thus representing the most poorly estimated series. This helps guide future sampling strategies, identifying those grid locations requiring additional information to reduce the uncertainties they introduce in the analysis. Somewhat surprisingly, we found that the error is more or less evenly distributed across all of the grid cells; perturbations in no one grid cell displayed a significantly larger influence than perturbations in any other grid cell.

4. Results

Our analysis findings are presented as follows: (1) results of the regional space/time variability as revealed by the EOF patterns and their PCs; (2) the covariability of these EOF patterns with indices and variables of extrapolar climate variability (teleconnections); (3) determination of the local/regional physical variables controlling the variations in the teleconnected characteristics. The consistency of the gridded data results at the various stages are evaluated through use of the uninterpolated super-data. These results are followed by a discussion of potential mechanisms explaining the observations over the variety of scales considered.

4.1 Gridded Data Analysis

4.1.1 Spatial/Temporal Variability.

Three leading EOFs lie above the noise floor for both Σ and $<F_T>$. These EOFs and their PCs, describing 43%, 20% and 9% of the total variance for Σ and 31%, 25% and 18% for $<F_T>$, are presented in Figure 4. The spatial distribution of the variance described by each EOF is determined by correlating the mode's PC to each cell in the gridded data ($\hat{\mathbf{T}}$). The fraction of variance explained for each grid cell is proportional to the EOF peak amplitude of that cell. Correlating the PC to the original super-data ($\mathbf{T}^o$), to the extent allowed by the super-data distribution, reveals similar r^2 spatial structure though poorer definition given the sparse data. However, in this latter case the southwest region of the gyre shows little explained variance, contrary to the case for the second and third modes of the gridded field. This suggests that the OA is imposing more coherent structure in the SW than actually exists in the data — likely a consequence of the particularly poor data density in that region of the grid. Consequently, we treat results arising from the gridded data in the SW region with considerable skepticism, and look to additional future data to help better constrain this portion of the domain.

The first two modes of both Σ and $<F_T>$ show similar spatial patterns and are clearly dominated by variability concentrated in the northern extent of the gyre. The EOF spatial structures (of coherent interannual variability) do not mimic the climatological patterns shown in *MI98*, though the latter does show considerable bulk property gradients through the northern rim of the gyre where it encroaches upon the subtropical regions. There is a reversed polarity between bulk stability's first EOF's amplitude in the NE and NW regions, while a comparable pattern in the first EOF of $<F_T>$ does not show the reversed polarity. The second mode EOFs, for both Σ and $<F_T>$ introduce a shorter wavelength fluctuation in the same northern region, though they also pick up the southwest (this latter influence presumably a consequence of the interpolation as stated above). Note that neither of the first 2 modes for either parameter describes much variability within the eastern core of the gyre, though even in the central western core of the gyre, the low amplitude of the first

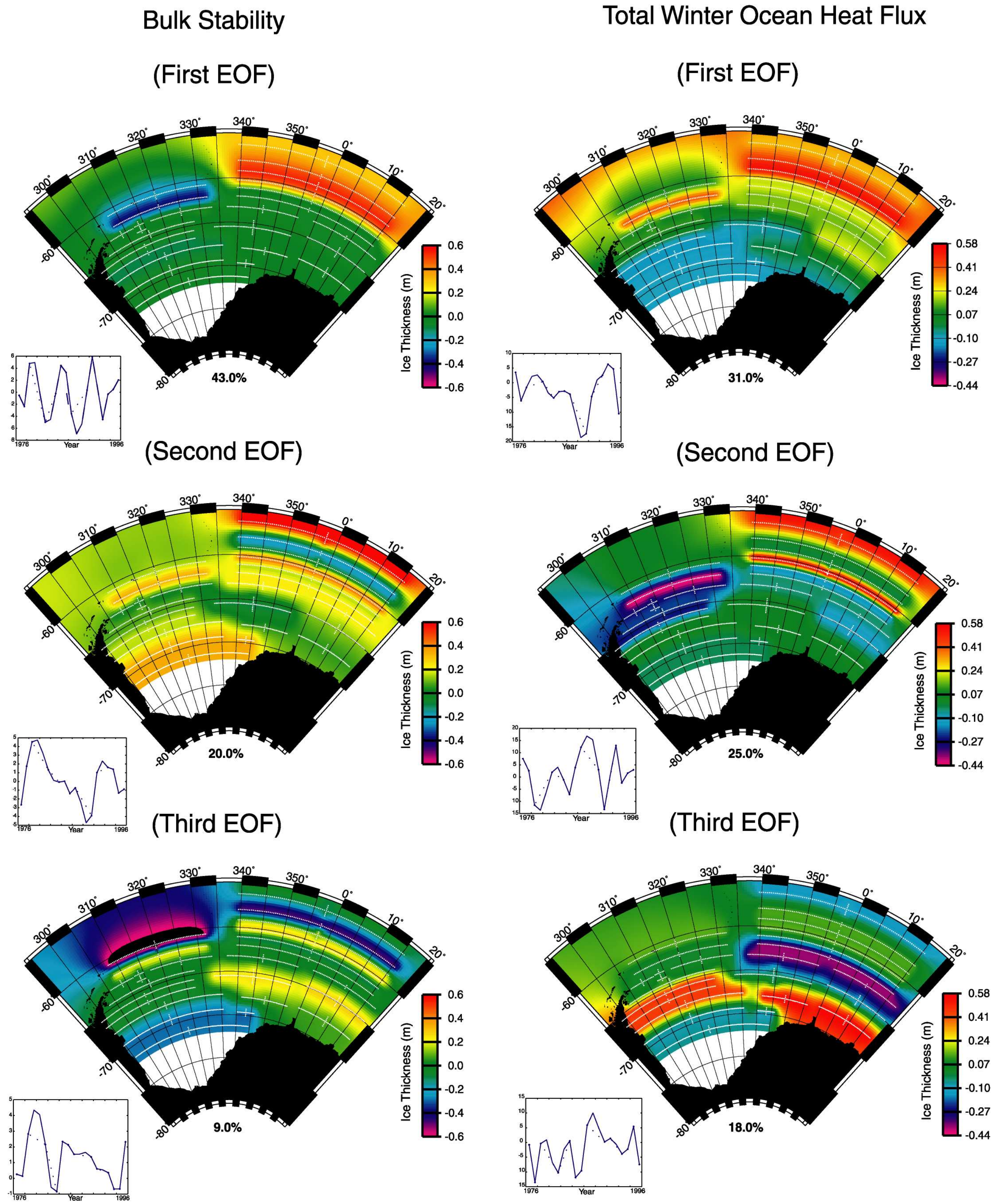

Figure 4. Lowest order modes, EOFs and PCs, for Σ and <F_T>. PCs, indicating amplitude of each EOF as it varies through time, are inset; percent total variance explained by each mode is indicated beneath EOFs. Notice color bars of standardized EOF amplitudes differ for Σ and <F_T>.

EOF accounts for ~40% of the total variance in that region. However, the third modes of each parameter do capture the gyre center with higher amplitude structure. They also add further refinement to the northern rim areas, but clearly the different PC variability suggests that the third EOF structure is adding more temporal stability to the short wavelength interannually-varying structure in the northern rim.

Examination of the temporal variability (PC) of the modal amplitudes shows that mode 1 is highly periodic, dominated by a narrow band 5-year cycle, whereas modes 2 and 3 are dominated by longer period trends persisting for approximately 10 years; e.g., Σ mode 2 decreases from 1978-1988; mode 3 from 1984-1994. For convenience, we will refer to these modes as showing decadal scale variability, recognizing that the series are too short to clearly define the time scale formally as such.

4.1.2 Circumpolar Teleconnections.

Now consider how the temporal variability of the Weddell modes covary with circumpolar SIE*. To evaluate this we correlated the detrended leading (3) PCs of Σ and $<F_T>$ to SIE* (of *YM00*) spanning the circum-Antarctic at 12° longitude non-overlapping windows. Correlations were computed over a broad range of lead/lag relationships, but because the bulk property parameters are integrated properties and sample cross correlation functions (ccf) have considerable smearing of the lags relative to the true ccf, lags $\leq|12|$ months are probably indistinguishable from those of 0 lag. Consequently, we only present lags of maximum correlations when they exceed $|12|$ months, or there is some other reason to assume them meaningful.

As exemplified by Figure 5, PC-SIE* correlations were typically strong in the Pacific sector and Weddell gyre region (e.g., r_{max} = -0.87 and 0.81 for PC2 of Σ and $<F_T>$, respectively in the western Weddell, with similar maximum r-values occurring for the other PCs and in the Pacific basins as well). At longer lead/lag times, a strong correlation is typically realized in the Indian Ocean center. These spatial patterns, as well as their space/time (lag) distribution reflect the geographic concentrations of coherent signal presented in Figure 4 of *YM00* when correlating SIE* to various extrapolar indices. However, here the patterns do not show the eastward propagation of r_{max} with lag, consistent with an apparently propagating SIE* anomaly field as expected with the Antarctic Circumpolar Wave of *White and Peterson* [1996]. Rather, we find a predominantly static or restricted eastward migration of anomalies. We do see strong evidence and clear delineation of the Antarctic Dipole of *YM00*. That feature is manifested by SIE* in the Amundsen/Bellingshausen Seas being strongly anti-correlated to SIE* of the western Weddell gyre region; the eastern Weddell, Drake Passage and Ross Sea regions are in-phase nodes enveloping the dipole — something clearly apparent in the correlation patterns here.

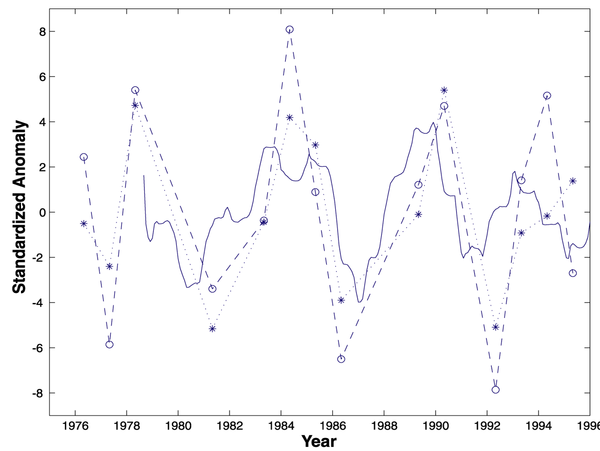

Figure 5. PC1 of Σ and $<F_T>$ superimposed on SIE* from Amundsen/Bellingshausen region to show nature of strong correlation (r_Σ=0.74; $r_{<F_T>}$=0.61).

The Antarctic Dipole signal is strongest in the PC2-SIE* correlations: there is a systematic change in the sign of r when moving eastward and crossing the boundary between the eastern Ross Sea and Western Amundsen Sea (at ~120° W), another sign change when crossing from the Bellingshausen Sea into the Western Antarctic Peninsula region (at ~70° W), and finally another sign change near the Greenwich Meridian, separating the eastern extension of the Weddell gyre (where the Circumpolar Deep Waters appear to enter the subpolar gyre) from the western portion. PC1 shows the clear delineation of the Amundsen/Bellingshausen and western Weddell, but not as systematically, and the broader coherent relationships with Ross Sea and eastern Weddell are not quite as clear as for PC2.

4.1.3 Extrapolar Teleconnections.

To evaluate the relationship of the Weddell OAI system modes to extrapolar climate, we examine correlations between PCs and global gridded SAT* and the 4 climate indices described in Section 2. The correlation results reflect many of the teleconnections of *YM00* for their case of extrapolar climate correlations involving SIE* in the Antarctic dipole region. Specifically, the strongest correlations for all PCs (see Figure 6) typically involve the ENSO region of influence, including the Pacific, Indonesia, western China, the tropical belt of the Indian Ocean/Africa. Like

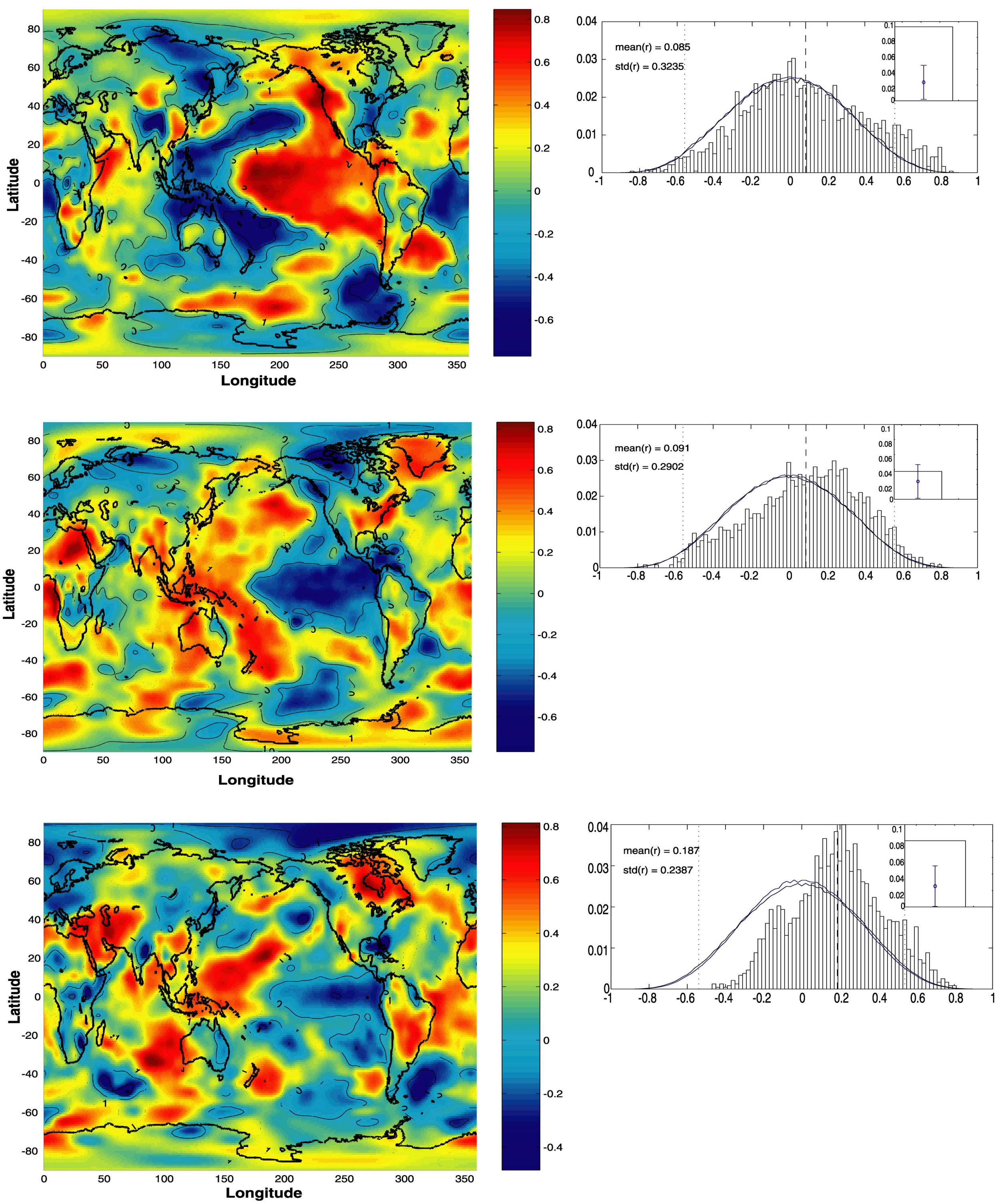

Figure 6. Correlation maps where colors reveal magnitude of correlation (r) between PCs 1-3 (a-c) for _ and time series of detrended near surface temperature anomalies (SAT^*) around the globe. Sample PDF for correlation map is compared to bootstrap PDF for each mode, to assess overall significance of correlations achieved. Significance of individual correlations are indicated by contours showing integer number of standard deviations from mean correlation value expected from bootstrap PDF generated for every global grid cell of SAT^*. Significance accounts for autocorrelations in space, time and multiplicity (see Appendix for discussion of significance).

YM00 we also find strong links to the Hudson Bay region, and regions near and/or encompassing southern South America, Africa and New Zealand. However, in the present case, the modes seem to show more consistent extrapolar regional foci than in *YM00*. Also, we find distinct patterns associated with each OAI mode, perhaps suggesting that each mode is linked to different extrapolar climate characteristics or represents a different mechanistic link. For all 3 modes the correlations peak at $r > |0.8|$. As above, lags are only stated when exceeding $|12|$ months, or there is some other reason to assume them meaningful. Statistical assessment of the correlation maps are presented in Figure 6 via confidence interval contours, whose derivation are described in Appendix 1.

The significance of the correlations are determined from the probability mass functions (called PDFs here though recognizing and treating them as *mass*, not *density*, functions) inset in Figure 6. The "sample" PDF for each correlation map is presented as a histogram and it reflects the distribution of r-values achieved in the PC versus SAT^* correlations presented by color-coding on the corresponding map of Figure 6. The more continuous-looking "bootstrap" PDF is generated using bootstrap techniques (see Appendix for discussion). It represents the distribution of r-values realized when generating 1000 correlation maps between SAT^* and colored noise instead of PCs. Conservatively, the colored-noise has the same spectral coloring (i.e., lower order statistical moments, autocovariance and quasi-periodicity) as the PCs used in the sample correlation.

Mode 1. This gravest mode appears to be a "global" mode, showing considerable (significant) covariability about the globe. Inspection of the correlation map (Figure 6a) reveals several interesting patterns of note. Foremost, the mode strongly captures the Antarctic Dipole of *YM00*, as well as its extension into the tropical Pacific and Atlantic. Specifically, the Amundsen Sea pole is in-phase with central tropical Pacific variability and the Weddell pole, of opposite sign to the Pacific pole, is in-phase with eastern tropical Atlantic variability. Meridional banding throughout the Atlantic from pole-to-pole, noted in *YM00*, is also captured particularly well by this mode, even in the highest northern extent. This suggests that one might expect to see good correlation between mode 1 and the NAO, but as discussed later, this correlation is not particularly strong. Finally there is strong covariability with the entire Western Pacific-Indonesian corridor, as well as strong regional links with each of the continents. The entire Pacific correlation pattern is reminiscent of the decadal ENSO signal region of influence, while the tropical Atlantic pattern is similar to that of the Tropical Atlantic Variability (TAV) region of influence, centered predominantly on the south equatorial branch of the TAV.

Statistically, this mode shows a significant positive shift in the mean r-value of the correlation map relative to that expected from the bootstrap PDF, as shown in the Figure 6a inset. However, the number of large r-values achieved globally (those in the upper 2.5% level of significance) are only 0.5σ more than to be expected from random chance involving colored-noise. We believe this reduced significance at highest r-values is a reflection of the strong periodicity inherent in this mode (nearly a perfect 5 year cycle). Thus, for noise with this dominant frequency band admitted (a conservative estimate), the noise's random phase implies that most of the random correlations will be of small correlation (thus not really altering the central body of the bootstrap PDF), but when the random phase of the narrow-band noise series is coincidentally similar to that of the climate variable (SAT^*), the alignment of the large variance frequency component will ensure a higher than otherwise expected r-value. This increases the relative frequency of occurrence of the highest r-values in the tails in the bootstrap PDF, tending to minimize the rarity of large r-values in the bootstrap correlations (and thus diminish the specific significance of the large r-value correlations achieved in the sample). Regardless, the significance at individual global gird cells (accounting for autocorrelation in space and time, and multiplicity) still show surprisingly widespread statistically-significant teleconnections.

Mode 2. The second mode appears to be more clearly an ENSO related mode, though it too shows global (significant) teleconnections (Figure 6b). In fact, this mode actually shows much of the same global distribution as mode 1, though here the teleconnections are of opposite sign than that of mode 1. Also for this mode the Pacific ENSO pattern is more significant and there is more concentration over the oceans, than in modes 1 and 3, which show more links to continental regions. The Antarctic Dipole is not as obvious in this mode and its Pacific branch, linking the Southern Ocean to the central Pacific is shifted westward to the Ross Sea.

The Atlantic branch, linking the Southern Ocean to central Atlantic is tied more strongly to the northern cell of the TAV pattern. It is interesting to note the similarity in patterns between modes 1 and 2 given the considerable difference in the dominant time scales of variability between PC1 and PC2, the former showing a strong interannual cycle and the latter more "decadal" variability. This not unlike the earlier findings of *Zhang et al*. [1997] who showed that when separating ENSO into its long (interdecadal) and short (interannual) time scales, the two components more or less respond at these unique time scales with similar regional patterns. Here too we seem to show a similar spatial distribution of teleconnections despite opposite signs and different time scales.

Statistically, the sample PDF for this mode shows a significant shift of the mean r-value toward more positive values, though this shift is more due to an extension of the high r-value tail of the sample PDF relative to that of the bootstrap PDF. Of the highest r-values (in the highest 2.5% of the PDF), the sample correlation map is ~3σ above those achieved through the 1000 bootstrap colored-noise correlation maps. Thus this mode seems to show a more overall teleconnection significance (i.e., overcoming problems of multiplicity) than mode 1.

Mode 3. Mode 3 shows (Figure 6c) elements of each of the two graver modes, though covariability with the Atlantic seems to dominate, with the Indian Ocean and Mesopotamia showing strong links as well. There are still clear signs of the ENSO Pacific pattern, but the significance is lowest in this mode relative to the other two modes, except in the western tropical Pacific where the correlation is high and the significance strong. This mode displays no indication of the Antarctic Dipole, but curiously shows a strong positive correlation to both pole regions of the Dipole

Statistically this mode shows the strongest and most significant nonzero mean correlation for the correlation map, even though visually the teleconnection pattern does not seem to be as broad as for the other two modes. The highest r-values occur in the upper 2σ range relative to the bootstrap PDF, and the overall most significant link is achieved with this mode and the Hudson Bay area of North America (r > 0.8, confident at > 2σ).

Climate Indices. We also investigate the relationship between the Weddell upper ocean characteristics and extrapolar climate variability as measured by the climate indices: NINO3, NAO, SOI and NPI (for PNA). Correlations significant at better than the 95% confidence limit include: (1) mode 1 does not show any particularly strong relationship (in term of explained variance) to any of these four, but achieves r = -0.54 with NPI and 0.51 with SOI; (2) mode 2 shows strong correlations with SOI (r = -0.7); and (3) mode 3 strongly covaries with NINO3 (r = -0.73) and with SOI (r = 0.64). While these show high significance, none show an overwhelming amount of shared variance, nor do they show stronger links than realized with the regional distributions of SAT^*. Therefore, we focus our discussion and interpretation primarily on the global SAT^* teleconnections in Section 5, below.

4.2 Super-Data (Non-Interpolated) Analysis

Having found widespread statistically-significant teleconnections between the OAI variability in the Weddell gyre region to extrapolar climate, we now investigate whether these correlations are an artifact of the OA interpolation. We do this by repeating some of the ENSO-related correlations using the (non-interpolated) super-data, instead of the gridded data. Motivated by the original results of Figure 1, the results of correlating NINO3 to the super-data as well as the OA gridded data are presented in Figure 7. Here correlation significance is not particularly relevant since we are more interested in examining the influence of the interpolation on the patterns and degree of correlations, hence we only focus on the nature of the relationship between super-data and gridded results.

The results are interesting from two perspectives. (1) The correlation patterns of Figure 7, are quite similar to the spatial pattern of EOF1, suggesting that the interpolation has not distorted the spatial patterns, other than its introduction of enhanced coherent structure in the SW region of the Weddell as previously noted. (2) The correlation patterns are similar for both the super-data and interpolated data suggesting that the OA interpolant has not introduced spurious coherent structure into the gridded data set. Furthermore, but perhaps more noteworthy, is that the correlations actually achieve higher r-values using the super-data than the gridded data. Examination of the correlated time series suggests that the reason for this is the filtering introduced by the reduced-space OA interpolant. That is, the interpolated series capture the broadest features, but the filtering has eliminated the subtle nuances present in each ENSO event. These are preserved in the super-data however, resulting in a higher degree of correlation (suggesting that the space reduction eliminated more ENSO-related signal variance than noise). Regardless, the preservation of the high degree of correlation with ENSO lends support to the fact that the gridded data present a reasonable approximation to missing values, and that the correlation results are not a methodological artifact. Similar results are achieved when comparing the correlation of specific SAT^* grid locations to the Weddell super-data and gridded data.

4.3 Local/Regional Physical Controls on Bulk Parameter Variability

In an attempt to identify plausible mechanistic links between the extrapolar variability and the Weddell OAI, we now wish to investigate what changes in the physical characteristics of the upper ocean water column are dominating the variability in the modes of Σ and $<F_T>$.

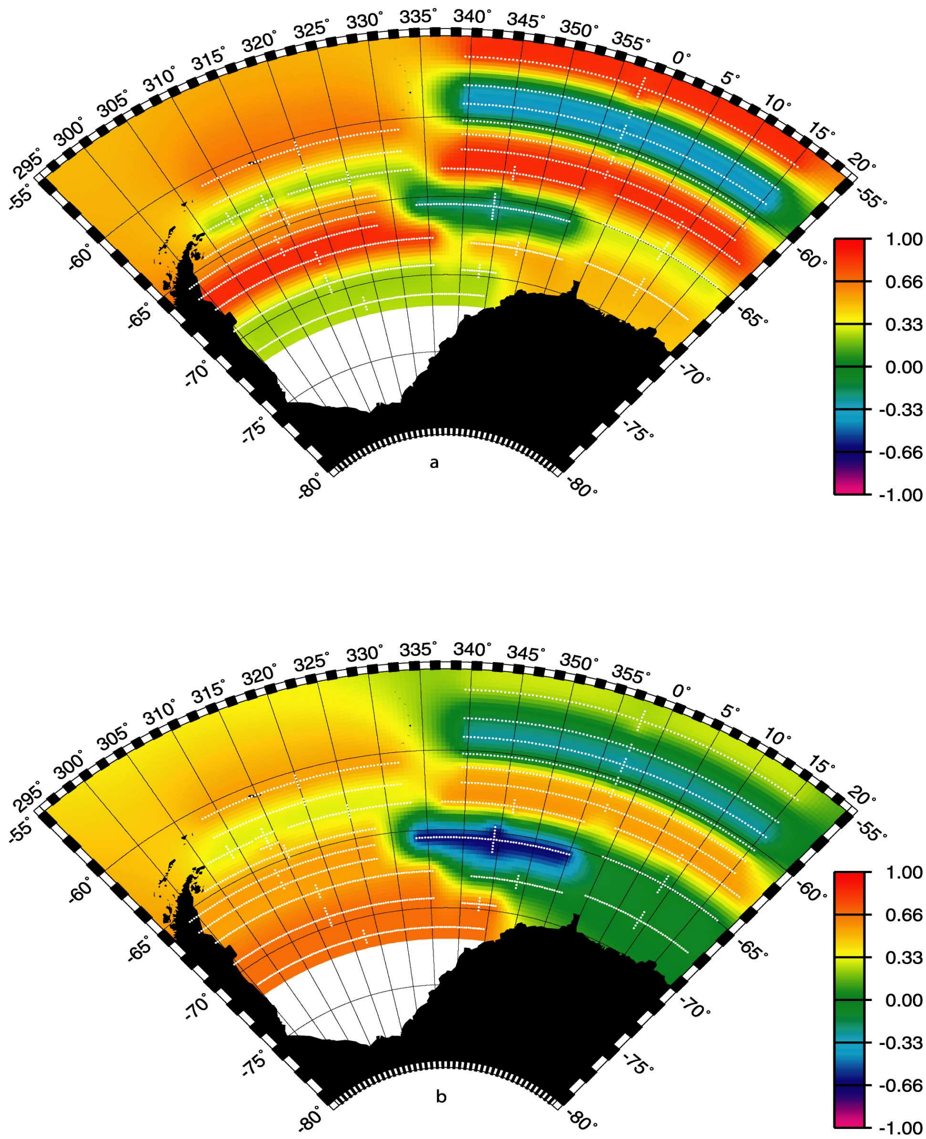

Figure 7. Correlation maps of NINO3 to Weddell gyre bulk stability using: (a) super-data (uninterpolated) and (b) OA interpolated data, with showing r for each grid cell.

Both of these OAI parameters are functions of SD_w and TB_w. $<F_T>$ has an additional dependency on $\overline{\nabla T}$ through the pycnocline. SD_w, TB_w and $\overline{\nabla T}$ are dependent upon the external system parameters: S_{ml}, z_{ml}, T_{pp}, S_{pp}, z_{pp} (T_{ml} is essentially invariant since its winter-average value is assumed fixed at the freezing point, so it is not considered here). Consequently, we wish to determine which of the external system (gyre-characteristic) parameters are dominating the bulk parameter variations and what mechanisms are consistent with those changes.

To investigate this dependence, we apply the OA on the 5 external system parameters and correlate the PCs of each of their gravest 3 modes to the dominant PCs of Σ and $<F_T>$. Interestingly, despite the different characteristic time scales of the different OAI modes, all 3 show a similar dominance of external parameter variability, though the relationships are considerably stronger and distinct for Σ relative to those for $<F_T>$.

The overwhelming majority of change is attributed to changes in TB_w (r^2 = 98%, 94% and 96% for PC1, PC2 and PC3, respectively) and to a lesser extent by SD_w (r^2 = 32%, 1% and 26% for PC1, PC2 and PC3, respectively). Note that the ascribed variance of TB_w and SD_w exceeds 100% of the variance, but this simply reflects covariability between TB_w and SD_w. The predominant control on SD_w (90% of the variance) is due to changes in the mixed layer salinity (S_{ml}) for mode 1. Mixed layer salinity is also the dominant control for mode 2, but at a significantly decreased level (14%). For mode 3, control is weakly distributed among mixed layer salinity and depth of the pycnocline.

For TB_w in mode 1, the dominant control is a change in temperature of T_{max} water (circumpolar deep water) at the base of the permanent pycnocline (describing 58% of the variance), with a lesser influence by a covarying change in T_{max} depth (25%). The increase in depth of T_{max} also influences the salinity gradient ($\overline{\nabla S}$, the halocline) and thus imparts an influence on SD_w as well, though this influence is only 25% (or a fraction of the influence imparted by S_{ml}). The change in salinity at T_{max}, while strongly correlated imparts no direct physical control on TB_w. For mode 2, changes in the depth of the pycnocline dominate (26%), with changes T_{max} playing a reduced role (~10%). For mode 3, the less distinct control on TB_w is still dominated by the depth and temperature of the T_{max} water (~14% each).

$<F_T>$ shows more evenly distributed control (74% and 63%) by TB_w and SD_w respectively, for PC1; a much smaller, albeit still even contribution for the other 2 modes. For mode 3 however, the control of TB_w and SD_w by the deep water characteristics (in this case, most evident by T_{max} characteristics, such as its depth, T and S) shows the opposite sign as found for the first mode. We find this opposite phasing physically consistent with our primary mechanism, as discussed below.

5. DISCUSSION

5.1 Mechanistic Interpretation of Observed Variability.

Analysis of the underlying cause of the variability in bulk stability, the bulk ocean-atmosphere-ice (OAI) parameter that displays the clearest relationship to physical characteristics of the upper water column, shows that its variability is dominated by changes in the thermal barrier, or excess enthalpy of the deep water. Changes in surface buoyancy altering the salt deficit play a lesser, but still important role. For all three modes the underlying physical changes driving the changes in TB_W and SD_W reflect variability in mixed layer salinity, and in the temperature and depth of the circumpolar deep water at the base of the pycnocline (or, of the T_{max} water). These physical changes covary in a manner that are consistent with changes in gyre vigor: increased winter-averaged cyclonic forcing either due to change in the Weddell climatological low pressure system, or due to a change in the fundamental nature of the storm distributions that ultimately define the climatological low.

The gyre-vigor changes are coherent with ENSO variability as defined by the broad teleconnection patterns, as in Figure 6. During El Niño events (tropical warming), the upper ocean response is consistent with an enhanced cyclonic forcing; diminished cyclonicity appears to accompany La Niña (tropical cooling) events. Increased cyclonic forcing leads to a contraction of the Weddell gyre, so at the northern rim of the gyre (represented by modes 1 and 2) the pycnocline is deeper (and warmer) as the gyre boundary migrates southward. This is consistent with climatologies of physical properties (computed for, but not shown in *MI98*) which reveal deeper, warmer and fresher (less dense) pycnocline-base (T_{max}) waters as one moves to the north in the circumpolar region. Thus, as the gyre contracts these waters migrate southward resulting in the deeper and warmer pycnocline-base (to T_{max}) waters occupying the northern rim region.

This relationship is strongest for mode 2, which, appears to show the clearest relationship to ENSO variability. Relative to mode 1, mode 2 is dominated by longer time-scale variability and shorter-wavelength features in its spatial pattern, though, like mode 1, it is concentrated in the northern rim of the gyre. For mode 1, the same physical variability dominates the changes in TB_w, but unlike mode 2, the salt deficit plays a considerable role in the coherent extrapolar covariability, and that is overwhelmingly controlled by changes in mixed layer salinity. This too is consistent with changes in gyre vigor. Enhanced cyclonic forcing and gyre contraction shows an increase in surface freshwater content, consistent with increased northward wind-driven ice transport associated with stronger northward divergence. This change is most prevalent in the interannual variability of PC1, and it may explain the broader wavelength northern rim EOF1 pattern, since the melting of wind-blown ice in the circumpolar region may be a broadly dispersed phenomenon.

Finally, mode 3, dominated by variability in the central gyre region and northwestern rim region, shows effects of opposite sign relative to the other two modes for the same change in regional forcing (e.g., enhanced cyclonic forcing shallows the pycnocline in the gyre center while decreasing it at the gyre edge). This opposite phasing is apparent in the relative sign of the EOF spatial pattern of Figure 4c. Because the EOF spatial pattern accommodates the anti-phasing of the dominant gyre regions of mode 3, the relationship of Σ to the deep water physical characteristic changes are similar to those discussed for modes 1 and 2, above. Likewise, the mode 1 variability with mixed layer salinity likely driven by wind-driven ice drift melt redistribution, is well apparent, though not as strong as for mode 1.

The mechanistic interpretation of the local/regional response of $<F_T>$ is not as clear as that of Σ. This may reflect the fact that $<F_T>$, in addition to being dependent on the same local upper ocean characteristics as Σ, has an additional dependency on air-sea heat flux (F_a). The latter is unobserved, and we are not yet confident that the reanalysis data properly capture its subpolar variability with enough fidelity to allow us to evaluate its co-dependencies. Thus, $<F_T>$ variability is not fully evaluated here, which confounds our ability to establish its physically-driven coherent behavior. Regardless, the covariability with OAI upper ocean characteristics for mode 1 are similar to the controls found for Σ, but of opposite phasing. That is, when the gyre is subjected to enhanced cyclonic forcing, the increased bulk stability works to reduce the ocean heat flux. This is consistent with the parameter dependencies of *MI98* and analysis of *Martinson*, 1990. It reflects that the ocean heat flux is more easily realized with weaker bulk stability, since that quantity reflects the potential energy that must be overcome to allow the surface waters to mix with the warmer underlying deeper waters (the heat flux in the Weddell region is dominated by entrainment of the pycnocline water, *MI98*).

The dominant changes in OAI modes 1-3 seem to be consistent with changes in gyre vigor: increased vigor for El Niño events, driving increased bulk stability and reduced ocean heat flux, and vice versa for La Niña events. These changes work to offset one another, so that the regional response tends to self regulate the already marginal stability of the system, though the results of Figure 1 show changes in $<F_T>$, when converted to the amount of ice growth reduction per year (units comparable to the bulk stability), that are approximately 3 to 10 times smaller than those of Σ. So, for El Niño associated increases in stability, the destabilization associated with the reduction in ocean heat flux is small relative to the stabilization of the water column indicated by the increase in Σ. This line of reasoning ignores covarying changes in the air-sea heat flux which may work to overcome these offsetting tendencies. For example, if the winter air-sea heat flux was stronger (e.g., the atmosphere is colder) during years of stronger bulk stability, it would work to enhance the influence of the weaker $<F_T>$, helping to overcome more of the increase in bulk stability. The details of this influence need to be evaluated once the air-sea heat flux, or atmospheric temperature over sea ice is adequately reconstructed.

These results are consistent with the earlier findings of *Carleton* [1988], and help constrain the nature of a local/regional mechanism by which the OAI system variability responds to ENSO forcing of the subpolar region. However, the analysis does not reveal how the ENSO variability is communicated across the hemisphere. *Peterson and White* [1998] suggest a slow ocean propagation of the tropical anomaly, though our results, particularly the instantaneous correlation results of Figure 1, suggest that the propagation may proceed much faster, implying an atmospheric mechanism. *Rind et al*. [submitted] find, through analysis of the Goddard Institute of Space Studies (GISS) GCM, that equatorial Pacific SST warm events (El Niño) lead to an increase in the Pacific pole-equator meridional temperature gradient. This intensifies the subtropical cell resulting in an equatorward shift of the subtropical jet (STJ). This shift displaces the SJT farther from the source of available potential energy in the Antarctic which leads to a reduction in cyclogenesis and overall storm intensity influencing the driving of the south Pacific subpolar ocean circulation. The equatorial warming also alters the Walker cell circulation leading to a reduction in tropical Atlantic subsidence. This alters the Atlantic's vertical meridional cell which introduces changes comparable to that as if the tropical Atlantic cooled and initiated a meridional temperature gradient in the Atlantic of opposite sign to that of the Pacific. The result is a relaxation of the Atlantic meridional circulation, accompanied by a poleward shift of the STJ poleward, closer to the available potential energy. This increases storm intensity in the Atlantic (Weddell) sector of the polar gyre, invigorating the cyclonic gyre, is consistent with the findings here. This hemispheric mechanism also explains the anti-phasing of the Antarctic Dipole, found here and in *YM00*, and is consistent with our broader understanding of Southern Hemispheric circulation and teleconnections, as summarized in the excellent review of *Carleton* [submitted]

5.2 Extrapolar Implications of Observed Subpolar Variability

The dominant covarying signals seem to be consistent with the ENSO connection and subpolar response discussed above. Other covarying characteristics are not as apparent or are buried in the noise. Thus it is not clear how the subpolar changes ultimately work to influence extrapolar climate. We assume that they do have such an influence based on previous modeling efforts that have found significant influences, without identifying the regional foci or underlying mechanisms, e.g., *Rind et al*., 1995. However, based on the response we have identified, we can speculate on how such changes may propagate elsewhere.

First, we see a strong subpolar response in the surface freshwater distribution in the circumpolar belt in response to changes in gyre forcing. Assuming an approximately balanced annual surface freshwater budget, the freshwater export at the northern rim of the gyre must balance the gyre's surface salt export, likely dominated by deep water formation along the southern continental margin of the gyre. Much of the northern freshwater flux is exported in the form of newly formed Antarctic Intermediate Water (AAIW). Presumably, if the surface winds alter the northern freshwater balance, this may impact the T-S characteristics and/or volume of the AAIW. The AAIW is an important body of water in the global heat balance primarily due to its shallow setting and influence on the heat exchange characteristics of the subtropical gyres [*Gordon*, 1991], thus influencing the upper ocean evolution and ultimately subtropical SST. The latter has an immediate and important impact on regional climate. Consequently, we hypothesize that subpolar regional changes induced by ENSO variability and operating over interannual time scales, may be propagated to longer time scales and broader space scales through its impact on the distribution and characteristics of the AAIW.

We expect a similar impact on deep water formation. Currently, it is assumed that much of the Antarctic deep and bottom water is formed via shelf convection and export along the northern tip of the Antarctic Peninsula [*Gordon et al*., 1993]. Deep water formation depends on the salinization along the shelves by ice growth followed by northern ice drift, so that the ice melts in the gyre interior leaving a destabilizing salt surplus on the shelves. The degree of ice formation and wind-driven export is tied to the strength of the cyclonic forcing: stronger forcing drives more offshore ice export, broader coastal polynyas, more ice production and destabilizing salt rejection, whereas weakened forcing leads to the opposite. A diminished forcing thus reduces the shelf salt surplus, and presumably the production of coastal deep water (though its production may be increased elsewhere in compensation). Furthermore, the reduction of ice drift into the gyre interior reduces the freshening there, favoring open ocean destabilization and convection (accompanied by polynya formation, altered air-sea heat exchange and surface albedo). The opposite is likely for enhanced cyclonic forcing. Here again, changes in deep water T-S characteristics and transports will influence the global heat balance on longer time scales and broader space scales, though the precise nature of the impact is not clear.

In the case of intermediate waters and deep/bottom waters changes, the changes are presumably slow enough that we would not expect to identify them in this correlation study given the limited length of observations (and it is questionable just how coherent such changes could be over the long time scales and broad diluting space scales).

Another potential feedback may develop through changes in the circumpolar cyclogenesis related to changes in sea ice extent (and shape) according to the feedback mechanisms of *Yuan et al*. [1999]. We find here that the gyre scale response in OAI characteristics covary with changes in ice edge extent, which in turn should enhance or diminish cyclogenesis. How that will feed back into the extrapolar climate is not clear however, though it will presumably influence the energetics of the meridional atmospheric circulation cells given its influence on the subpolar jet.

5.3 Additional Insights

Consistent with *YM00* we show a predominant correlation of gyre characteristics with regionally-emphasized locations throughout the circumpolar belt (as well as elsewhere on the globe). But, in that previous work, there is clear manifestation of an eastward propagation of the correlated anomalies, whereas here, they appear to be more stationary. This is an interesting finding and it may indicate that the gyre interior is varying in a manner more consistent with standing wave variability in the sea ice extent anomalies while the extrapolar indices are linked to a moving wave feature that radiates out from the standing wave peaks. If this is true, it has implications regarding the mechanism and interactions of the ACW, ACC, regional dynamics and the atmospheric standing wave field (i.e., it tends to link all of the major features of the circumpolar region through one interesting constraint). It may also indicate that the gyre interior signal does not show the longevity of the extrapolar climate indices and circumpolar region, and thus the anomalies do not persist long enough to show up significantly in the progressive lagged correlations required to capture the eastward migration of SIE^* anomalies (i.e., the cross correlation decorrelation length is short).

Correlation analysis included an examination of correlations over a broad range of lead and lag relationships. However, the interpretation of lags involving the bulk parameters and their physical implications is difficult for two reasons: (1) the bulk parameters are computed from T and S profiles, collected during a specific time, but that time is independent of the physical interpretation of the bulk parameter. For example, if the profile is taken in summer, we compute the bulk stability by essentially stripping away the overlying summer freshwater cap and seasonal pycnocline. Thus, we compute the bulk stability that will constrain the winter seasonal evolution, once fall cooling and initial ice growth eliminate the seasonal pycnocline. We compute the winter-averaged ocean heat flux in the same manner, so the values computed from summer (or any other season) profiles reflects the average heat flux that is expected in the upcoming winter. Thus the bulk parameters are typically representative of subpolar winter conditions, regardless of the time of year the profiles are collected. (2) Even given a winter emphasis, the temporal influence of the parameter varies according to the parameter. For example, bulk stability indicates how resistant the water column is to overturning. As such, it is an indication of a threshold value, rarely realized. From this perspective, one would interpret Σ as a diagnostic of vertical stability, reflecting the nature of the seasonal evolution from the seasons preceding the winter for which the value is representative of — it therefore represents a response to previous regional forcing and gyre characteristics. Heat flux on the other hand, while also set by the preceding seasonal evolution, reflects a parameter that will have a distinct influence on the winter for which it is computed (the upcoming or current winter relative to the timing of the profiles from which it is computed). For example, an increase in ocean heat flux implies a year (ignoring changes in the air-sea heat flux) that will grow less ice, show weaker upper ocean destabilization and pycnocline erosion, and presumably will warm the lower subpolar atmosphere. Therefore, the different bulk parameters have different physical implications and interpretations, and their direct relationship to a lagged correlation is muddled as a consequence.

This is further confounded by the considerable error in an autocorrelation or cross correlation function, whose sample estimates are equivalent to the true cross correlation function convolved with itself. In other words they are subjected to considerable smearing, which adds uncertainty to the precise lag at which the correlation peaks. Finally, physical interpretation of the causal implications of a lead/lag relationship is questionable given the quasi-periodic nature of the climate series used here (though they can still be exploited for predictive purposes). For these reasons, in this initial study we did not attempt to interpret leads/lags.

6. Conclusions

This study seeks to improve our documentation and understanding of polar-extrapolar teleconnections and the mechanisms by which they are communicated across the hierarchy of scales involved (local, regional and global). We improve the documentation by investigating how the local-scale ocean-atmosphere-ice (OAI) interactions within the subpolar Atlantic sector of the Southern Ocean (Weddell gyre region) covary with extrapolar climate variability. We quantify climatically-meaningful OAI interactions through the robust parameters of *Martinson and Iannuzzi* [1998]. These parameters involve integrated upper ocean properties, and they are externally controlled by the broader, regional scale gyre dynamics. As such, the parameters tend to link the subpolar local and regional scales together.

The sparse and sporadic nature of the subpolar data inhibits our ability to directly perform comprehensive and systematic analyses. We overcome this limitation by employing the optimal analysis (OA) of *Kaplan et al.* [1998]. This yields an internally-consistent gridded data set with an enhanced signal-to-noise ratio (reflecting the reduced-space of the optimal interpolant). Coherent spatiotemporal OAI structure is isolated through an Empirical Orthogonal Function (EOF) analysis which is performed as part of the optimal analysis. Most of the variance of the 25-year gridded data set is contained in the first three (well separated) spatial EOFs (explaining >70% of the variance). Examination of these lowest order EOFs reveals that coherent gyre-scale spatial covariability of the upper ocean bulk stability (Σ) and seasonally-averaged winter ocean heat flux ($<F_T>$) is dominated by high interannual variability near the northern (circumpolar) rim of the gyre, with lesser, slower variability in the gyre interior and southern sections (dominating the third mode).

Temporal variability of the EOF spatial patterns is described by the Principal Components (PCs). The PCs of the leading modes were correlated to: (1) detrended sea ice extent anomalies (SIE^*) around the Antarctic in order to determine the relationship between gyre-interior OAI interactions and circumpolar sea ice extent; (2) detrended surface air temperature anomalies (SAT^*) from the NCEP/NCAR global reanalysis data to determine the extent and regional distribution of the OAI variability with extrapolar climate variability; and (3) indices representing the major global or hemispheric scale climate phenomena, such as ENSO, PNA, NAO and SOI.

The correlations reveal the following. (1) The Weddell gyre interior OAI system seems to covary most strongly with SIE^* in the Amundsen/Bellingshausen and Weddell gyre regions, reflecting the Antarctic dipole of *Yuan and Martinson* [2000]. (2) Extrapolar climate variability is most clearly dominated by a teleconnection with ENSO variability. In global correlations with SAT^* the ENSO regions of influence consistently arise as regions of strongest (and significant) covariability. This is reinforced by covariability revealed through correlations with a standard ENSO index (NINO3). Statistical evaluation of the correlations via bootstrap techniques accounts for autocorrelations in space and time, and the problem of multiplicity, which reflects the fact that given enough correlations, one must expect occurrence of even the low-likelihood (high r-value) correlations to occur. We find considerably more strong correlations (exceeding 95% confidence) than expected from chance (even allowing for noise to display the same spectral coloring as the data, including highly autocorrelated quasi-periodic components). We investigate the likelihood that our results contain methodological-induced artifacts by repeating a subset of the correlations using the original uninterpolated data and find this not to be the case. The correlations appear to be robust, though the gyre-scale spatial variability within the Weddell OAI fields appears to display more coherent structure in the particularly data-sparse and inaccessible SW region of the Weddell Sea, than is apparent in the original uninterpolated data — this does not appear to alter our teleconnection findings, nor their mechanistic interpretation.

Finally, in an attempt to understand how the local/regional OAI system variability may be mechanistically linked to ENSO variability, we identified those particular changes in the upper ocean that were responsible for the dominant covariability present in the OAI bulk parameters. Of the 5 upper ocean characteristics that control the bulk parameters, two dominated the observed variability: mixed layer salinity (S_{ml}), and circumpolar deep water temperature and depth (T_{pp}, z_{pp}), as measured at the base of the permanent pycnocline (or at T_{max}). The S_{ml} changes are most pronounced in the northern rim of the gyre where it is most sensitive to sea ice drift and melt; there, S_{ml} increases during El Niño years and decreases during La Niña years. T_{pp} and z_{pp} increase at the northern rim of the Weddell gyre and decrease in the gyre center in El Niño years, with an opposite response for La Niña years. This variability is consistent with increased cyclonic forcing of the Weddell gyre during El Niño years and diminished cyclonic forcing in La Niña years. It is also consistent with modeling analyses of *Rind et al.* [submitted] who find that equatorial Pacific SST warm events (El Niño) lead to an increase in the Pacific pole-equator meridional temperature gradient which intensifies the subtropical gyre resulting in an equatorward shift of the subtropical jet (STJ). This shift displaces the SJT farther from the source of available potential energy in the Antarctic which leads to a reduction in cyclogenesis and overall storm intensity (particularly in the Amundsen and Bellingshausen Sea region that lies in the southernmost Pacific). The equatorial warming also perturbs the Walker cell circulation leading to the opposite response in the Atlantic. This hemispheric mechanism also explains the anti-phasing of the Antarctic Dipole.

The results presented here demonstrate the feasibility and usefulness of applying the optimal analysis to the sparse and sporadic subpolar Weddell upper ocean data. A more detailed analysis can be made once improved multi-year upper ocean sampling of the Weddell allows for a finer resolution and better defined construction of the gyre covariance structure. The latter argues for future sampling strategies whereby gyre-scale surveys are re-occupied over multiple years to further define the gyre's covariance structure and make better use of the historical data. Once the structure is defined, maintenance surveys are periodically required to monitor the stability of the covariance structure (samples near the EOF dominant amplitude locations provide the most valuable information, *Evans*, 1999). Also, the exceptionally sparse sampling of the SW portion of the Weddell gyre makes its contribution to the overall gyre variability poorest, so additional future CTD profiles from this region would be of particular benefit. The advantage of the bulk property parameters employed in this study is that they can be derived from profiles taken at any time of the year (with summer being optimal, despite the fact that they describe winter system interactions).

Acknowledgments. This research was supported by National Science Foundation grant: OPP 96-15279 (ANZFLUX experiment) and a National Ocean and Atmosphere Administration grant/cooperative agreement (UCSIO P.O. 10075411). Sea ice extent anomalies used herein were derived by *Yuan and Martinson* [2000a] using the SMMR-SSM/I and SSM/I F13 sea ice concentration data provided by the National Snow and Ice Data Center. The individual correlation maps of Figure 4 were plotted using GMT, by *Wessell and Smith*, 1991. The authors benefited from discussions with Xiaojun Yuan, and with Alexey Kaplan regarding the best way to treat the particularly sparse data being analyzed here via his optimal analysis technique.

References

Ackley, S.F., M. Lange and P. Wadhams, Snow cover effects on Antarctic sea ice thickness. In, *Sea Ice Properties and Processes: Proc. of the W.F. Weeks Symposium*, S.F. Ackley and W.F. Weeks, eds., CRREL Monograph 90-1, 16-21, 1990.

Cane, M. A., S. E. Zebiak and S. C. Dolan, 1986: Experimental forecasts of El Nino. *Nature,* 322, 827-832.Carleton, A.M., Sea-ice atmosphere signal of the Southern Oscillation in the Weddell Sea, Antarctica, *J. Clim.,* 1, 379-388, 1988.

Carleton, A.M., ENSO Teleconnections with Antarctica, *J. Geophys. Res.,* submitted.

Chiu, L.S., Antarctic Sea Ice Variations 1973-1980, in *Variations in the Global Water Budget*, edited by A. Street-Perrott et al., 301-311, D. Reidel Publishing Company, 1983.

Evans, M., Sea Surface Temperature Field Reconstruction from Coral Data: Methodology and Application. Ph.D. Thesis, Columbia University, 117 pp., 1999.

Fletcher, J.O., U. Radok, and R. Slutz, Climatic signals of the Antarctic Ocean, *J. Geophys. Res.,* 87, 4269-4276, 1982.

Fletcher, J.O., Ice extent in the southern oceans and its relation to world climate. *J. Glaciol.* 15, 417-427, 1969.

Gloersen, P., Modulation of hemispheric sea ice covers by ENSO events, *Nature*, 373, 503-508, 1995.

Gordon, A.L., Seasonality of Southern Ocean Sea Ice, *J. Geophys. Res., 86*, 4193-4197, 1981.

Gordon, A.L., Two stable modes of Southern Ocean winter stratification, in *Deep Convection and Deep Water Formation in the Oceans*, eds. Chu and Gascard, Elsevier Science Publishers, 17-35, 1991.

Gordon, A.L., The Southern Ocean: Its Involvement in Global Change, in *Proceedings of the International Conference on the Role of the Polar Regions in Global Change*, edited by V.G. Wall, C.L. Wilson, & B.A.B. Severin, 249-255, University of Alaska, Fairbanks, 1990.

Gordon, A.L. and B.A. Huber, Thermohaline stratification below the Southern Ocean sea ice, *J. Geophys. Res.*, 89, 641-648, 1984.

Gordon, A.L., and B.A. Huber, Southern Ocean winter mixed layer, *J. Geophys. Res.*, 95, 11655-11672, 1990.

Gordon, A.L., B.A. Huber, H.H. Hellmer and A. Ffield, Deep and bottom water of the Weddell Sea's western rim, *Science,* 262, 95-97, 1993.

Hansen, J.E., M. Sato, R. Ruedy, A. Lacis, and J. Glascoe, Global Climate Data and Models: A Reconciliation, *Science*, *281*, 930-932, 1998.

Hines, K.M. and D.H. Bromwich, The roles of Arctic and Antarctic sea ice in forcing global climate. *Fifth Conference on Polar Meteorology and Oceanography*, 39-43, 1999.

Imbrie, J., E.A. Boyle, S.C. Clemens, A. Duffy, W.R. Howard, G. Kukla, J. Kutzbach, D.G. Martinson, A. McIntyre, A.C. Mix, B. Molfino, J.J. Morley, L.C. Peterson, N.G. Pisias, W.L. Prell, M.E. Raymo, N.J. Shackleton & J.R. Toggweiller. On the Structure and Origin of Major Glaciation Cycles. 1. Linear Responses To Milankovitch Forcing. *Paleocean.*, 6, 701-738, 1992.

James, I.N., On the forcing of planetary-scale Rossby waves by Antarctica, *Q. J. R. Meteorol. Soc.*, 114, 619-637, 1988.

Kalnay, E. and Coauthors, The NCEP/NCAR 40-year reanalysis project, *Bull., Amer. Met. Soc.,* 77, 437-471, 1996.

Kaplan, A., M.A. Cane, Y. Kushnir, A.C. Clement, M.B. Blumenthal, and B. Rajagopalan, Analyses of global sea surface temperature 1856-1991, *J. Geophys. Res.*, 103, 18567-18589, 1998.

Karoly, D.J., Southern Hemisphere Circulation Features Associated with El Niño-Southern Oscillation Events, *Amer. Met. Soc.*, 2, 1239-1252, 1989.

Katz, R.W. and B.G. Brown. The Problem of Multiplicity in Research on Teleconnections, *Inter. J. Climatol.*, 11, 505-513, 1991.

Kellogg, W. W., Climatic feedback mechanisms involving the polar regions. *Climate of the Arctic*, G. Weller and S. A. Bowling, Eds., Geophysical Institute, University of Alaska Fairbanks, 111-116, 1975.

Krishnamurti, T.N., S.-H. Chu, and W. Iglesias, On the Sea Level Pressure of the Southern Oscillation, *Arch. Met. Geoph. Biocl.*, Ser. 34, 385-425, 1986.

Large, W.G., and H. van Loon, Large-scale, low frequency variability of the 1979 FGGE surface buoy drifts and winds over the Southern Hemisphere, *J. Geophys. Res.*, 19, 216-232, 1989.

Ledley, T.S., and Z. Huang, A Possible ENSO signal in the Ross Sea, *Geophys. Res. Lett.*, 24, 3253-3256, 1997.

Lemke, P., A coupled one-dimensional sea ice-mixed layer model, *J. Geophys. Res.*, 92, 13164-13172, 1987.

Martinson, D.G., and R.A. Iannuzzi, Antarctic ocean-ice interaction: implications from ocean bulk property distributions in the Weddell Gyre, In: *Antarctic Sea Ice: Physical Processes, Interactions and Variability*, Ant. Res. Ser., V74, AGU, Washington, D.C., 243-271, 1998.

Martinson, D.G., Evolution of the Southern Ocean winter mixed layer and sea ice: open ocean deepwater formation and ventilation., *J. Geophys. Res.*, 95, 11641-11654, 1990.

Massom, R., and J. Comiso, The classification of Arctic Sea ice types and the determination of surface temperature using advanced very high resolution radiometer data, *J. Geophys. Res.*, 99, 5201-5218, 1994.

McPhee, M., C. Kottmeier, and J. Morison, Ocean heat flux in the central Weddell Sea during winter, *J. Phys. Ocean.*, 29, 1166-1179, 1999.

Meehl, G.A., A Reexamination of the Mechanism of the Semiannual Oscillation in the Southern Hemisphere, *J. Clim.*, 4 , 911-926, 1991.

Mitchell, J.F.B., and T.S. Hills, Sea-ice and the Antarctic winter circulation: A numerical experiment, *Quart. J. R. Met. Soc.*, 112, 953-969, 1986.

North, G.R., T.L. Bell, R.F. Calahan, and F.J. Moeng, Sampling errors in the estimation of empirical orthogonal functions, *Mon. Wea. Rev.*, 110, 699-706, 1982.

Parish, T.R., The Influence of the Antarctic Peninsula on the Wind Field Over the Western Weddell Sea, *J. Geophys. Res.*, 88 , 2684-2692, 1983.

Peterson, R.G., and W.B. White, Slow oceanic teleconnections linking the Antarctic Circumpolar Wave with the tropical El Niño- Southern Oscillation, *J. Geophys. Res.*, 103, 24,573-24,584, 1998.

Rind, D., R. Healy, C. Parkinson, and D. Martinson, The role of sea ice in $2XCO_2$ climate model sensitivity, I, The total influence of sea ice thickness and extent, *J. Clim.,* 8, 449-463, 1995.

Rind, D., M. Chandler, J. Lerner, D.G. Martinson, X. Yuan. Latitudinal Temperature Gradients and Sea Ice Response. *J. Geophys. Res.*, submitted. [preprint available on web at: http://rainbow.ldgo.columbia.edu/]

Ropelewski, C.F., and M.S. Halpert, Global and regional scale precipitation patterns associated with the El Nino/Southern Ocean Oscillation. *Mon.Wea.Rev.*, 115, 1,606-1,626, 1987.

Shapiro, R., The use of linear filtering as a parameterization of atmospheric diffusion, *J. Atmos. Sci.*, 28, 523-531, 1971.

Simmonds, I. and M. Dix, The circulation changes induced by the removal of Antarctic sea ice in a July general circulation model. *Proc. Second Int. Conf. On Southern Hemisphere Meteorology*, New Zealand, Amer. Meteor. Soc., 107-110, 1986.

Simmonds, I., and T.H. Jacka, Relationships between the interannual variability of Antarctic sea ice and the Southern Oscillation, *J. Clim.,* 8, 637-647, 1995.

Simmonds, I., and D.A. Jones, The Mean Structure and Temporal Variability of the Semiannual Oscillation in the Southern Extratropics, *Int. J. Climatol.*, 18, 473-504, 1998.

Simmonds, I. and M. Dix, The circulation changes induced by the removal of Antarctic sea ice in a July general circulation model. *Proc. Second Int. Conf. On Southern Hemisphere Meteorology*, New Zealand, Amer. Meteor. Soc., 107-110, 1986.

Simmonds, I., and R. Law, Associations Between Antarctic Katabatic Flow and the Upper Level Winter Vortex, *Int. J. Climatol.*, 15, 403-421, 1995.

Simmonds, I., and X. Wu, Cyclone behaviour response to changes in winter southern hemisphere sea-ice concentration, *Q.J.R. Meteorol. Soc.*, 119, 1121-1148, 1993.

Stammerjohn, S.E., and R.C. Smith, Opposing Southern Ocean Climate Patterns as Revealed by Trends in Regional Sea Ice Coverage, *Clim. Chang.*, 37, 617-639, 1997.

Trenberth, K.E., W.G. Large, and J.G. Olson, The mean annual cycle in global ocean wind stress. *J. Pohys. Oceanogr.*, 20, 1742-1760, 1990.

van Loon, H., The Southern Oscillation. Part III: Associations with the trades and with the trough in the westerlies of the South Pacific Ocean, *Mon. Wea. Rev.,* 112*,* 947-954, 1984.

van Loon, H., and D.J. Shea, The Southern Oscillation. Part IV: The Precursors South of 15°S to the Extremes of the Oscillation, *Mon. Wea. Rev.*, 113, 2063-2074, 1985.

van Loon, H., and R.L. Jenne, The Zonal Harmonic Standing Waves in the Southern Hemisphere, *J. Geophys. Res.*, 77, 992-1003, 1972.

Walker, G.T., 1923: Correlation in seasonal variations of weather, VIII. *Mem. Ind. Meteor. Dept.*, 24, 75-131.

Walsh, J.E., The Role of Sea Ice in Climatic Variability: Theories and Evidence, *Atmosph - Ocean*, 21, 229-242, 1983.

Wessel, P. and W.H.F. Smith, Free software helps map and display data, *EOS Trans. Amer. Geophys. U.,* 72, 441, 445-446, 1991.

White, W.B., and R.G. Peterson, An Antarctic circumpolar wave in surface pressure, wind, temperature and sea-ice extent, *Nature, 380,* 699-702, 1996.

White, W.B., S.-C. Chen, and R.G. Peterson, The Antarctic Circumpolar Wave: A Beta Effect in Ocean-Atmosphere Coupling over the Southern Ocean, *J. Phys. Oceanogr.*, 28, 2345-2361, 1998.

Yuan, X., D.G. Martinson, and W.T. Liu, Effect of air-sea-ice interaction on winter 1996 Southern Ocean subpolar storm distribution, *J. Geophys. Res., 104,* 1991-2007, 1999.

Yuan, X. and D.G. Martinson, 2000a. Antarctic sea ice variability and its global connectivity. *J. Clim.*, 13, 1697-1717.

Yuan, X., and D.G. Martinson, Predictability of the Antarctic Dipole, *Antarctic Weather Forecasting Workshop Volume*, Byrd Polar Research Center, Ohio State University, Columbus, OH, May 2000, 2000b.

Zhang, Y., J.M. Wallace and D.S. Battisti, ENSO-like decade-to-century time scale variability: 1900-93, *J. Clim.*, 10, 1004-1020, 1997.

Appendix

A.1 Correlation Significance

The statistical significance for the correlations in Figure 1 and Figure 6 (as well as all other correlations not shown) is determined by bootstrap, or resampling, statistics. This involves synthesizing multiple noise series which preserve the lower order univariate and bivariate statistical moments of the actual OAI time series being used in the correlations. We preserve the mean, variance and noise-related autocovariance via a linear power law fit to the Power Spectral Density function (PSD) of the real time series. For irregularly space series, such as the OAI time series of Figure 1 and correlations involving the original super-data which contains gaps, we compute the PSD by computing a least squares fit of a Fourier series to the original n unevenly spaced data points with harmonics generated assuming a sampling interval, $\Delta t = \overline{\Delta t}$, and period, $T = n\Delta t$. The linear power law preserves the noise-autocovariance for most forms of natural noise, including white, red, flicker (1/f) and fractal. However, we also repeat the bootstrap assessments preserving the complete PSD structure which admits any quasi-periodic components in the data series as being inherent in the noise itself. This is unnecessarily conservative (particularly for those cases in which the time series is dominated by one or two narrow band spectral peaks, such as for PC 1). By comparing the statistical significance of this approach to that of the linear power law, we can assess the role played by the quasi-periodic components in the strength of the teleconnections. We find that in most cases the bootstrap PDF did not differ by much, perhaps a small amount in the extremes of the tails of the distribution. We generate multiple realizations of colored-noise time series that preserve the statistical moments of the sample OAI series by inverting the noise spectra using random (pseudo-white noise) phase, though preserving the phase symmetry required of real series. We generated 1000 evenly-spaced colored noise time series in this manner, to evaluate each correlation (5000 noise series for index correlations, such as that done in Figure 1). When testing unevenly-spaced sample series, the colored-noise series were resampled (decimated) to the original temporal uneven sampling interval of the data, thus preserving the autocorrelation and accounting for the effective degrees of freedom of the original values at their sampled time intervals.

For correlations to indices, such as NINO3, each of the 5000 colored-noise series was then correlated to the index and the distribution of the r-values accumulated in a "bootstrap" PDF as presented in Figure 1a. We evaluated the significance of the sample correlation achieved between the index and sample OAI series by integrating the bootstrap PDF to the r-value of the sample correlation.

For correlation maps like those in Figure 6, each of the 1000 colored-noise series was correlated to the global gridded SAT*, producing a bootstrap correlation map (consisting of ~2600 individual correlations per map). The PDFs of r-values for each individual bootstrap map were then combined to provide an accumulative bootstrap PDF (consisting of ~2.6 million individual bootstrap correlation estimates). The PDFs thus account for autocorrelation in space and time, but unlike the situation of correlations to climate indices, discussed above, here we cannot simply read the significance of a correlation for any particular grid cell directly from the PDF because of the problem of multiplicity [*cf. Katz and Brown*, 1991]. Multiplicity states that given enough correlations we would expect to reproduce the full PDF of r-values, including the rarer high r-values. We account for multiplicity in the following manner: (1) we first evaluate the mean of the sample PDF and compare it to the mean of the accumulative bootstrap PDF. This indicates whether there is a significant shift from 0 (the mean of the bootstrap PDFs) in the sample correlations. (2) we evaluate if we have more high-r values in our sample correlation map (those exceeding the upper 95% of the distribution) than expected from the bootstrap PDF (taking into account the scatter realized in the individual bootstrap PDFs — this scatter is presented in the form of a standard deviation error bar superimposed on the accumulative bootstrap PDF presented in the Figure 6 PDF insets). This indicates that even given multiplicity arguments we are realizing more strong correlations than expected, even allowing for the vast number of correlations. (3) Finally, given positive results for the first two tests, we utilize the bootstrap statistics accumulated for each individual grid cell on the global correlation maps to assign the confidence interval of the r-values achieved at each individual grid cell. The confidence interval is contoured on the correlation maps at 1σ (standard deviation) intervals. Note that the confidence intervals closely follow the r-values, but they need not do so since the scatter (σ) in bootstrap r-values at each grid cell differ (they do differ by about a factor of 2, but this introduces only minor deviations from an otherwise linear relationship between the sample r-value and its significance).

As expected, the bootstrap PDFs generated by preserving the entire sample PSD for the noise PSD leads to longer tails in the PDFs. This reflects that fact that even though the noise contains the quasi-periodic components present in the data, they are synthesized with random phase, to that for most noise realizations the quasi-periodic components are not phase-aligned with their sample series counterpart, and therefore do not contribute to enhancing the sample r-value. However, in those random instances where the phase is aligned, they can increase r considerably. This explains why these PDFs contain more density in the tails, and tend to diminish the significance of the large r-value correlations that are obtained in the sample correlation maps. Even so, we still obtain a preponderance of large r-values in the sample maps, more so than expected from quasi-periodic colored-noise.

The statistics for the presented correlations are discussed in the text with the results, but two statistical insights are readily apparent (and presented) in the comparison of the inset PDFs for the correlation maps of Figure 6. In each case, the sample mean r-value is significantly different from the bootstrap mean value of zero (t-test determined level of significance). This indicates a larger degree of non-zero correlations than expected if the correlations were simply a consequence of random chance (based on the bootstrap colored-noise series). Also, the sample PDFs consistently show more high (low-probability) r-values than expected from the bootstrap PDFs, though for mode 1, the higher number is less than a full standard deviation above the mean for high (95% confidence) r-values. The predominance of high r-values in the sample correlation relative to that expected from the colored-noise indicates that we are achieving more large correlations than expected by random chance. However, because we are performing so many correlations, we cannot simply delimit the r-values associated with some predefined level of significance on the bootstrap PDFs to assign correlation significance (though this does account for autocorrelation in space and time). Rather the considerable number of correlations computed for each PC-SAT* correlation map mandates that we would expect to see the entire PDF of r-values realized, including the rarer large values; this is the problem of multiplicity. We evaluate the 1000 individual bootstrap PDFs, to assess the likelihood of achieving as many high (≥97.5% confidence) r-value correlations as we realized in the sample PDF; there is only a 0.1% chance of receiving that many high values from random chance assuming colored-noise. This is consistent with multiplicity arguments [*Katz and Brown*, 1991] that indicate the largest r-values are the ones that are most significant (and likely to represent a causal relationship) relative to what is expected from noise.

A.2 Instantaneous Correlation

We evaluate the details of individual correlations, such as those of Figure 1, by investigating the distribution of correlated pairs contributing to the overall r-value achieved in the correlation. How the correlation is accumulated provides useful insights when considering mechanisms responsible for the correlation. For example: (1) large r as the result of consistently good correlation throughout the entire time series may suggest that the causal mechanism linking the two series is operating full time; (2) large r as the result of strong correlation for limited high-variance events with weak correlation at other times may suggest that the causal mechanism is only operating (or is operating more efficiently) when some threshold state is exceeded [see *Yuan and Martinson*, 2000b, for such a case]; or, (3) large r as a result of just one or two exceptionally large variance events may suggest that the correlation is rather meaningless mechanistically if limited to just a single exceptional variance event, though a threshold mechanism could still be a possibility.

We quantify this correlation distribution with an instantaneous (sample) correlation coefficient, $r_i^{\prime}$, defined when correlating two series, **X** and **Y**, as

$$r_i^{\prime} = \frac{(x_i-\bar{x})(y_i-\bar{y})}{s_x s_y} \quad \text{(A.1)}$$

where the overbar indicates sample mean, and s_z indicates sample standard deviation for series **Z**. In this manner, the sample correlation coefficient is given as

$$r = \sum_{i=1}^{n} r_i^{\prime} \quad \text{(A.2)}$$

Thus, $r_i^{\prime}$ provides an indication of how each pair of points in the two series being correlated, at time t = i, contribute to the overall correlation. For other uses, we normalize $r_i^{\prime}$ so as to account for the natural elevation of values associated with large amplitude events, but here this normalization is not warranted for the investigation of interest.

The expectance operator allows us to determine the population and sample statistics moments, but we find that they require simplification by linearization and an assumption of weak stationarity (covariance does not change with time through the series) in **X** and **Y** in order to collapse to useful standard forms (e.g., the population mean $\overline{\rho_i^{\prime}} = \rho/n$, where ρ is the population correlation). Also, in the absence of rigorous assumptions regarding the distribution of $r_i^{\prime}$ we would be limited to assessing significance of through application of the overly conservative Chebyshev's inequality. We prefer to avoid these simplifying approximations and work with actual significance, so we again rely on the bootstrap to directly establish the applicable statistical moments and assess significance. The stationarity assumption is inappropriate since we are investigating a single realization of climate. Thus each different sample-based realization of climate is presumably a variant on the one "true" climate signal, and thus we can expect particular high-variance years to always be high-variance years given some scatter, etc. (i.e., we are dealing with the question of signal to noise). More importantly we must expect large variance events to contribute more to r than small events (regardless of the causal relationship). We can accommodate this by either normalizing to the deviation at each time point, or, as we prefer, to investigate the Z-scores of r'_i, which automatically accounts for the original variance of the individual data points. These statistics are presented as a mean and 1 standard deviation error bar in the instantaneous chart presented in Figure 1. As seen, the bootstrap mean is comparable to the population mean of r/n, and where we achieve large r' they are still significantly different than expected from the bootstrap distributions.